A flexible high-precision photoacoustic retinal prosthesis

Audrey Leong†, Yueming Li†, Thijs R. Ruikes†, Julien Voillot, Yuhao Yuan, Guo Chen, Arnaud Facon, Chakrya-Anna Chhuon, Corentin Joffrois, Gilles Tessier, Marion Cornebois, Julie Dégardin, Jean-Damien Louise, Ji-Xin Cheng*, Chen Yang*, Hélène Moulet#*, Serge Picaud#*.
† equal contributions, # equal contributions

A. Leong, T.R. Ruikes, C. Joffrois, G. Tessier, M. Cornebois, J. Dégardin and S. Picaud*
Institut de la Vision,
Sorbonne Université, INSERM, CNRS,
Paris, 75012, France
Email: serge.picaud@inserm.fr

Y. Li, Y. Yuan, G. Chen, J-X Cheng*, C. Yang*
Department of Electrical and Computer Engineering,
Boston University,
Boston, MA, 02215, United States
Email: jxcheng@bu.edu; cheyang@bu.edu

J. Voillot, A. Facon, C-A Chhuon, J-D Louise, H Moulet*
Axorus SAS,
Loos, 59120, France
Email: helene.moulet@axorus.com

Author Contributions

AL, YL and TRR contributed equally to this work.

HM, J-DL, J-XC, CY and SP conceived the project and contributed to study design, data interpretation and revision of the manuscript.

AL, YL, TRR, JV and HM contributed to sample preparation, data collection, analysis and interpretation.

CJ contributed to sample preparation (ex vivo experiments).

AF and C-AC contributed to data collection (ex vivo and in vivo experiments).

YY and GC acquired the `3D profile of the photoacoustic field.

JD and MC performed the in vivo surgeries, OCT imaging, and contributed to data interpretation.

GT contributed to data interpretation (thermal effects).

AL, YL, TRR and HM wrote the manuscript with input from all others.

Abstract

Retinal degenerative diseases of photoreceptors are a leading cause of blindness with no effective treatment. Retinal prostheses seek to restore sight by stimulating remaining retinal cells. We here present a photoacoustic retinal stimulation technology. We designed a polydimethylsiloxane and carbon-based flexible film that converts near-infrared laser pulses into a localized acoustic field, aiming at high-precision acoustic activation of mechanosensitive retinal cells. This photoacoustic stimulation of wild-type and degenerated ex vivo retinae resulted in robust and localized retinal ganglion cell activation with sub-100-µm resolution in both wild-type and degenerated ex vivo retinae. Our millimeter-size photoacoustic film generated neural activation in vivo along the visual pathway to the superior colliculus, as measured by functional ultrasound imaging when the film was implanted in the rat subretinal space and stimulated by pulsed laser. Biosafety of the film was indicated by absence of short-term adverse effect under optical coherence tomography retinal imaging, while local thermal increase was measured below 1 °C. These findings demonstrate the potential of our photoacoustic stimulation for visual restoration in blind patients with a high spatial precision and a large field of view.

Introduction

Retinitis pigmentosa and age-related macular degeneration affect millions of people worldwide[1]. These conditions result in an irreversible photoreceptor degeneration and blindness. Currently, there is no effective drug treatment for preventing photoreceptor loss. Retinal prostheses are implantable devices designed to activate the remaining retinal layers to restore vision without the need for genetic modification[2]. Currently, the design of clinically tested retinal prostheses and their impact on patients are extremely limited. Only two types of retinal prostheses, which both primarily use electrostimulation to restore vision, have been approved for commercial implantation[3], but both have been removed from the market after around five hundred patients were implanted worldwide. These prostheses are facing challenges, such as poor spatial resolution and small restored visual field, and are not able to provide satisfying outcomes in patients. For example, the electrode-based Argus II retinal prosthesis (Second Sight, USA, now merged with Nano Precision Medical, USA) is composed of 60 pixels with a spatial resolution larger than 250 µm. Photovoltaic-based PRIMA (Pixium Vision, FR, recently acquired by Science Corporation, USA) is one of the most advanced retinal prostheses still in clinical trials (NCT04676854). It has 378 pixels and offers a resolution of 100 µm. PRIMA has been shown to restore a median 20/500 visual acuity in AMD patients with profound vision loss[4]. While this is a remarkable achievement, patients remain legally blind. In addition, due to the design of rigid solid-state devices, PRIMA is limited to 2 mm in size and currently provides a very limited restored visual field of 7°.

Other retinal stimulation methods alternative to prostheses have been recently developed. Optogenetics allows selective stimulation of transfected cells at single-cell precision[5]. By transfecting the RGCs with a microbial opsin, optogenetic restoration of retinal ganglion cell activity has recently been developed[6–8] and tested in a clinical study (NCT02556736[6]). Yet, this method requires genetic modification via AAV transfection[6–8], which currently limits the field of view of the restored visual perception to the perifoveal ring[8,9]. At the preclinical level, focused ultrasound has also been explored as an exciting noninvasive method for retinal stimulation[10]. For example, the Baccus Lab has shown a piezoelectric transducer with a focal spot diameter of 90 µm that evokes stable responses in the salamander retina[11]. The Zhou lab reported non-invasive focused ultrasound retinal stimulation in the RCS rats, a model of retinal dystrophy, with a spatial resolution of 250 µm[12–14]. Unfortunately, the mechanical index needed for such a focused ultrasound retinal stimulation is reported to be 10-100 times higher than FDA mechanical index safety threshold of 0.23 for ophthalmological use[12], imposing safety concerns.

Photoacoustic modulation is an emerging non-genetic method for high-precision neural stimulation[16,17]. It uses a photoacoustic converter activated by a pulsed laser to generate localized ultrasound, offering high spatial precision and multiplexing capacity via photons. High spatial resolution stimulation of individual neurons has been demonstrated through a fiber-based photoacoustic emitter[16]. Moreover, a biocompatible and flexible silk-based photoacoustic film has been developed for modulation of neurons or neural tissues cultured on the film[18].

In this study, we investigated photoacoustic retinal stimulation as an alternative strategy for restoring vision at the retinal level. We here provide evidence of its efficacy both *ex vivo* and *in vivo* on the healthy and degenerated retinae and the biosafety of the photoacoustic implant in short-term implantation.

Results

Fabrication and characterization of the flexible photoacoustic film

The working principle of photoacoustic retinal stimulation is illustrated in Fig. 1A. A near infrared (1030 nm) pulsed laser is delivered to the back of the eye onto the retina, illuminating the subretinally-implanted flexible photoacoustic film. The nanosecond laser absorbed by the photoacoustic (PA) film produces transient heat and generates pulsed ultrasound. The generated ultrasound activates the remaining retinal cells, facilitating vision restoration.

The PA film is composed of candle soot (CS) as the absorber material, sandwiched between two layers of polydimethylsiloxane (PDMS), which serves as the thermal expansion material (implant design is further outlined in the Discussion). The photoacoustic PDMS/CS/PDMS film was fabricated via flame synthesis and spin coating methods (Fig. 1B). The film has a Young's modulus of 2.12 ± 0.10 MPa, which provides flexibility that may help to minimize the immune response[19,20] when used as an implant (Supplementary Fig. S1). Photoacoustic properties of the PA film were characterized with a hydrophone placed 0.9 mm away from the film (Fig. 1C). Upon excitation with 7 µJ laser pulses, the PDMS/CS/PDMS film emitted ultrasound pulses with peak-to-peak pressure of 146.2 kPa, resulting in a conversion efficiency of 21 kPa/µJ. At the surface of the film, the conversion efficiency is estimated at 63 kPa/µJ based on the decaying profile shown in Fig. 1D and previous study[21] (*Supplementary Materials, section 1.2*). The latter conversion efficiency is consistent with the efficiency reported in previous study of a carbon soot-based fiber photoacoustic emitter[21]. The film produced PA signals with a central frequency of 42.2 MHz and -6 dB bandwidth ranging from 29.6 to 59.9 MHz. This central frequency has been demonstrated to activate e*x vivo* salamander retinae with a lower intensity threshold compared to lower acoustic frequencies[22]. Taken together, the high conversion efficiency and optimal frequency of the PDMS/CS/PDMS film suggest that it is a promising photoacoustic converter for photoacoustic stimulation.

The spatial distribution of the ultrasound field generated by the PDMS/CS/PDMS film was further mapped by PA field microscopy (Fig. 1D). A 50-µm optical fiber was positioned in contact with the PA film to assure a 50-µm illumination area. The axial pressure profile shows that the maximum pressure is generated at the surface of the film upon illumination (Z = 0 µm) and attenuates to 50% of its peak value at Z = 140 µm (Fig. 1D, right). The lateral width (W) of the acoustic field, quantified by the full width at half maximum, measures W = 56 µm at Z = 0 µm and increases with axial depth to W = 124 µm at Z = 100 µm (Fig. 1E). Noticeably, a side lobe is present to the right of the field due to the slight tilted angle when the optical fiber was put in contact with the sample film. These results

confirm that under a confined illumination, the PA film produce a highly localized, sub-100-µm ultrasound field laterally, opening up potential for retinal stimulation with sub-100-µm resolution.

To demonstrate that we can control the generated pressure by varying the incident laser energy, we measured the acoustic pressure generated at laser pulse energy ranging from 1 to 10 µJ. Acoustic pressure exhibited a linear relation with the laser pulse energy (Fig. 1F), which indicates that the output pressure can be precisely modulated by adjusting the input laser energy.

Finally, to ensure that the ultrasound generation with the designed PA film is not associated with a substantial temperature increase, we measured the temperature at the surface of the PA film. The tested laser conditions used were consistent with those employed in the following *ex vivo* retinal stimulation experiments (next section). We observed a maximum temperature rise of 0.52 ± 0.09 °C (Fig. 1G). The baseline change due to cumulative thermal effects was 0.20 °C after 40 s. This value is an order of magnitude below the temperature increase needed to thermally activate neurons[23,24]. Therefore, the film is unlikely to thermally activate retinal neurons.

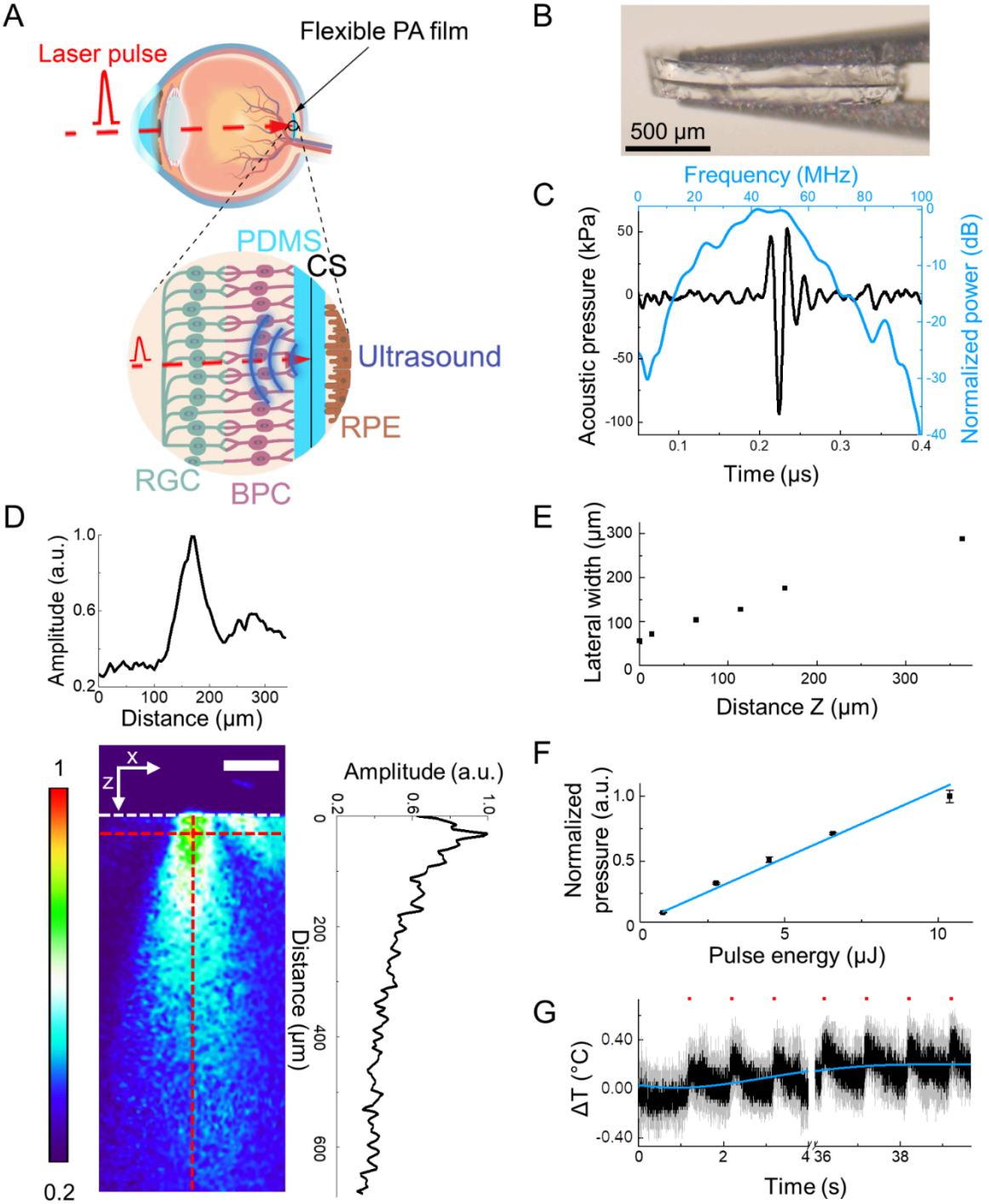

Figure 1. Characterization of the flexible photoacoustic film. (A) Working principle of the flexible photoacoustic (PA) film. A laser pulse (red dashed line) activates the photoacoustic film (cyan), which then emits ultrasound (blue). CS: candle soot, PDMS: polydimethylsiloxane, RPE: retinal pigment epithelium, RGC: retinal ganglion cells, BPC: bipolar cells. **(B)** A photograph of the three-layer design of the PDMS/CS/PDMS film. **(C)** PA performance in the temporal domain (black) and frequency domain (blue) of the photoacoustic film shown in B. A 1030-nm laser delivered 8 ns pulses with an energy of 7 µJ per pulse. **(D)** Mapping of the ultrasound field generated by the PDMS/CS/PDMS film upon illumination through a 50-µm optical fiber. *Center*: distribution of the generated US field

measured by a pump-probe method. *Top and right*: normalized lateral and axial profiles of the PA pressure, respectively, measured along the red dashed lines in the center panel. The amplitude of the acoustic signal was normalized to the maximum amplitude measured in the field. White dotted line: interface between water and film. Scale bar: 100 µm. **(E)** Full width at half maximum of the lateral profile as a function of the axial position Z extracted from panel D. **(F)** PA peak-to-peak pressure as a function of laser pulse energy measured from a PDMS/CS/PDMS film by a hydrophone. Distance between the film and the hydrophone was 0.9 mm. The pressure was normalized to the maximum pressure in all the measurements. N = 3 for each data point. Blue line: linear fitting: $y = 0.105x$, $R^2 = 0.9945$. **(G)** Temperature increase at the surface of the PA film following illumination with a 200-µm laser spot. N = 3 for each data point, mean (black line) ± SD (grey shade). Red dots: laser on. Laser parameters: energy of 10 µJ/pulse, repetition rate of 3 kHz (laser power density P = 0.95 W/mm²), and burst duration 50 ms, delivered every 1 s over 40 s by a 200-µm diameter optical fiber. Maximum temperature rise of 0.52 ± 0.09 °C. The baseline change because of cumulative thermal effect was obtained by applying a low-pass filter function to the data (blue line).

Photoacoustic activation of the ex vivo retina

To evaluate the retinal responses following photoacoustic retinal stimulation, we recorded the activity from the retinal ganglion cells (RGCs) of *ex vivo* retinae from wild type Long Evans (LE) rats on a multi-electrode array (MEA) (n = 4 rats, 559 cells). The PDMS/CS/PDMS film was placed against the photoreceptor layer of the *ex vivo* retina. The film was photoactivated by delivering a 1030-nm pulsed laser through a 200-µm optical fiber placed at a fixed distance (~1 mm) above the PA film (Fig. 2A). The illumination spot on the film was ~300-µm in diameter. The fiber was moved to different recording sites (n = 11 sites) between simulations. We applied laser pulses in short bursts of burst duration d_b = 10 ms, repetition rate of 1.9 kHz, and pulse energy of 10 µJ (Fig. 2B, top), corresponding to a power density of P = 0.27 W/mm². Under such laser conditions, the PA film generated a central frequency of 42 MHz, and an estimated peak-to-peak ultrasound pressure of 0.28 MPa based on the linear relationship between laser energy and pressure established in Fig. 1F.

Photoacoustic stimulation evoked robust RGC responses in healthy LE retinae (see example data in Fig. 2B and Fig. 2C, top two panels). RGCs were considered responsive or activated if their firing rate significantly increased (excitatory response) or decreased (inhibitory response) relative to baseline. We found that 71% out of the spontaneously active RGCs within the stimulation range (<300 µm from stimulation site, LE: n = 176 cells) showed an altered activity under photoacoustic stimulation (Fig. 2E). RGC response dynamics were heterogeneous (Fig. 2D, left), being either excitatory (red, 81% of responsive RGCs) or inhibitory (blue, 19% of responsive RGCs). Excitatory RGCs responded with a mean firing rate of 56 ± 24 Hz (mean ± SE), which was significantly higher than the baseline firing rate (15 ± 0.66 Hz, Fig. 2F), and had a mean response latency of 55 ± 39.5 ms (Fig. 2G). 50% of LE cells were fast responding, with response latency below 45 ms. The response latency was inversely correlated with firing rate, with short latency responses having high firing rates, and long latency responses having lower firing rates (Fig. 2H).

To investigate the potential of photoacoustic stimulation for restoring vision, we then measured the photoacoustic-elicited responses in *ex vivo* retinae from blind P23H rats aged 10 to 12 months (n = 4 rats, 258 cells). Similarly to LE retinae, P23H cells had robust responses to the photoacoustic stimulation (Fig. 2C, bottom two panels), but a lower fraction of spontaneously active RGCs showed a modified activity (34% out of 258 RGCs within stimulation range, Fig. 2E). Fewer cells exhibited an inhibitory response (blue, 6% of responsive RGCs), and the majority of responsive cells had an

excitatory response (red, 94 % of responsive RGCs, Fig. 2D, right). The firing rate of cells with excitatory responses was also significantly increased compared to baseline (Fig. 2F), but the mean firing rate after stimulation was significantly smaller for P23H cells (29 ± 2.88 Hz) than in LE cells (Fig. 2G). The mean response latency increased in P23H cells to 90 ± 66.2 ms compared to LE cells (55 ± 39.5 ms). Only 36% of P23H RGCs had a response latency below 45 ms, which was significantly less than for LE cells (50%, Fig. 2G). Taken together, these results suggest that the short-latency responses may be mediated by photoreceptors. These results demonstrate the *ex vivo* efficacy of the photoacoustic stimulation in activating retinal ganglion cells from the degenerated retina.

We then investigated the mechanotransduction pathway in the degenerated retina, by applying glutamatergic blockers (rs)-CPP and CNQX to P23H retinae (Fig. 2I). Baseline activity of cells was reduced following bath-application of the synaptic blockers, while the PA-induced responses were nearly completely abolished. PA-induced responses recovered following washout of the blockers (Fig. 2I). These results suggest that the main mechanosensitive cells are upstream of RGCs, and that glutamate neurotransmission is required to transfer the mechanosensitive signal to the RGCs.

Finally, to exclude the possibility that RGCs were activated by light transmitted through the film (which absorbs 99% of the laser energy, *Supplementary Fig. S4*), we applied laser pulses on the bare LE retina next to the PA film. Using 10 ms laser bursts, a repetition rate of 3.5 kHz and laser pulse energy of 10 µJ, only 3.6 ± 0.9% RGCs showed a modified activity under the off-film laser stimulation, while on-film stimulation reached 77 ± 20% modified activity in RGCs (Fig. 2J). This result confirms that the observed RGC responses upon laser activation of the photoacoustic film was not caused by a direct photostimulation of the retina.

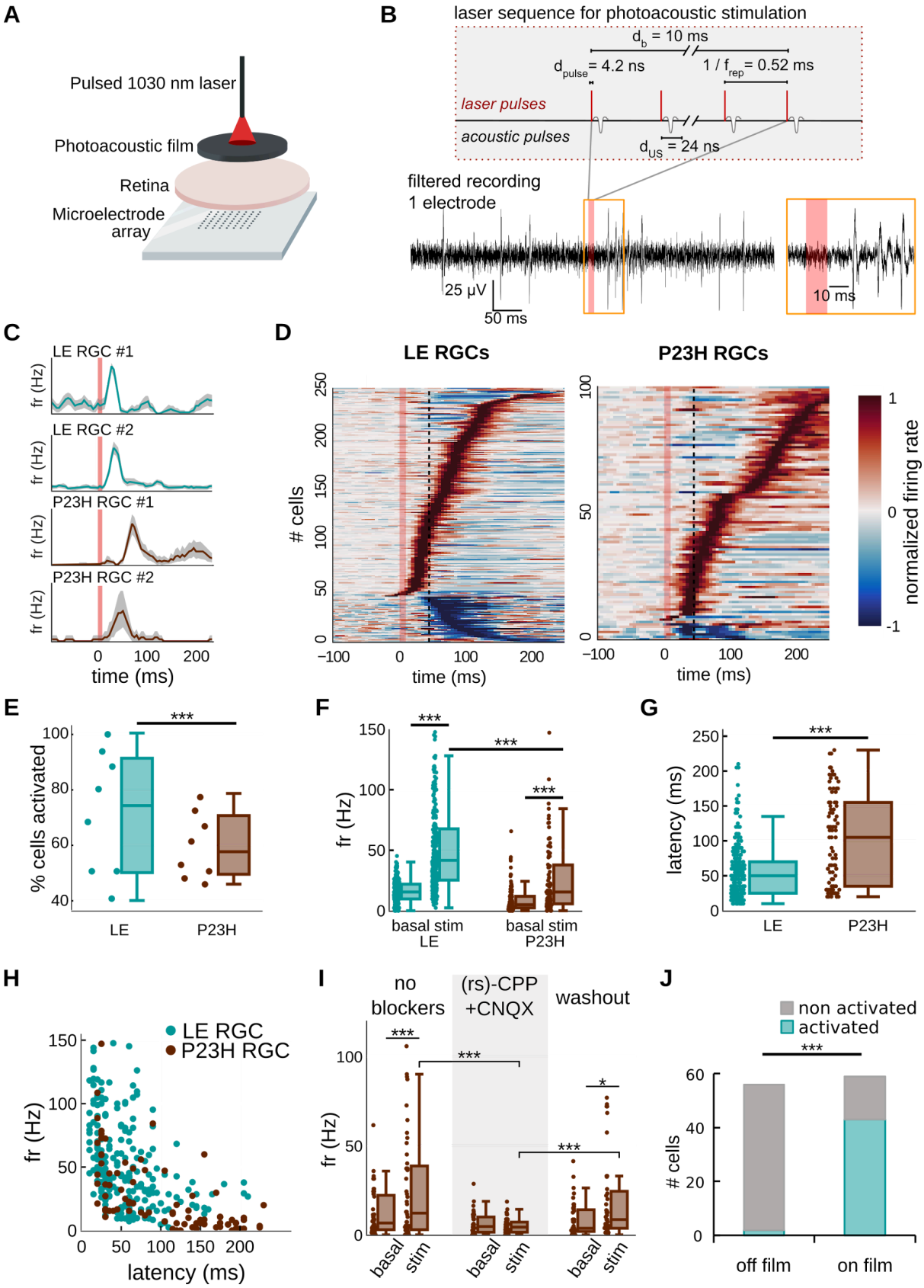

Figure 2. Photoacoustic activation of ex vivo wild type and degenerated retinae. (A) The *ex vivo* retina was placed on a multielectrode array with the photoacoustic film on top. The film was activated with a 1030-nm pulsed laser. **(B)** *Top*: schematic of laser sequence for photoacoustic

stimulation. Laser pulses, with energy 10 µJ per pulse and duration d_{pulse} = 4.2 ns, were delivered at a repetition frequency f_{rep} = 1.9 kHz during a single burst of duration d_b = 10 ms. Each laser pulse is converted by the PA film into an acoustic wave with a duration T = 36 ns. *Bottom*: Example high-pass filtered MEA recording from a single electrode displaying activity following photoacoustic stimulation. Red shaded area: laser on. Right inset: action potentials following stimulation. **(C)** Examples of Long Evans (LE) and P23H RGC mean responses to photoacoustic stimulation. Black: mean firing rate. Gray shaded areas: 99% bootstrapped CI from 1000 samples. Red shaded area: laser on. **(D)** Heatmaps of normalized firing rates for cells activated by photoacoustic stimulation. Left: LE RGC responses (n = 256 cells, 4 retinae, cells outside stimulation range included). Right: P23H RGC responses (n = 108 cells, 4 retinae, cells outside stimulation range included). Red shaded areas: stimulation period. Dashed black line: 45 ms cutoff for slow and fast latency responses. Excitatory cells display an increase in firing rate after photoacoustic stimulation (red), inhibitory cells display a decrease in firing rate (blue). **(E)** Percentage of cells activated by photoacoustic stimulation per stimulation site, RGCs within a range of 300 µm were included. LE: 71 % (4 rats, n = 10 stimulation sites), P23H: 34 %, (4 rats, n = 12 stimulation sites). *** $p < 0.001$, Mann Whitney U test. **(F)** Firing rates of LE and P23H RGCs during baseline (basal) and following stimulation (stim). Mean firing rates: LE: fr_{basal} = 15 ± 0.7 Hz, fr_{stim} = 56 ± 2.4 Hz (n = 185 RGCs within stimulation range, $p < 0.001$, Wilcoxon signed-rank); P23H: fr_{basal} = 10 ± 1.2 Hz, fr_{stim} = 27 ± 2.81 Hz (n = 91 RGCs within stimulation range, $p < 0.001$, Wilcoxon signed-rank). **(G)** Latencies of RGC responses for LE (55 ms ± 39.5ms, mean ± standard deviation) and P23H (95 ms ± 68 ms). **(H)** Firing rate of activated RGCs as function of response latency. Firing rate and response latency of excitatory RGCs were correlated for LE ($r = -0.452$, $p < 0.001$, Pearson correlation) and P23H ($r = -0.559$, $p < 0.001$, Pearson correlation) RGCs. **(I)** Glutamate blockers (rs)-CPP+CNQX abolish RGC responses to photoacoustic stimulation in P23H retinae. Population firing rate of RGCs (n = 44 cells, 2 retinae) is compared between baseline (basal) and stimulation (stim), before admission (no blocker), following admission ((rs)-CPP+CNQX) and after washout (washout) with RINGER medium. Firing rate per condition, *none*: fr_{basal} = 12 ± 13 Hz, fr_{stim} = 26 ± 29 Hz ($p < 0.001$); (rs)-*CPP+CNQX*: fr_{basal} = 6 ± 6 Hz, fr_S = 6 ± 4 Hz ($p = 0.749$); *washout*: fr_{basal} = 8 ± 9 Hz, fr_{stim} = 21 ± 27 Hz ($p = 0.021$). Comparison of population stimulation firing rate fr_{stim} following blocker admission and fr_{stim} before admission ($p < 0.001$, Wilcoxon signed-rank), and fr_{stim} after washout $p < 0.001$ (Wilcoxon signed-rank). **(J)** Photoactivation control. Percentage of RGCs activated by direct laser stimulation on the retina ("off film") compared to photoacoustic stimulation ("on film"). Laser parameters: d_b = 10 ms, f_{rep} = 3.5 kHz, E_p = 10 µJ/pulse. Off film: 3.6% ± 0.9% (n = 56 cells 2 retinae), on film: 77% ± 20% (n = 59 cells, 3 retinae). Statistics: * $p < 0.05$, *** $p < 0.001$, , Mann-Whitney U-test.

Dependence of RGC response on laser conditions

We further investigated the RGC responses upon photoacoustic stimulation using different laser repetition rates and burst durations. LE and P23H retinae were stimulated by delivering 1030-nm laser in bursts of durations (d_b) ranging from 5 to 30 ms, at 10 µJ per pulse and two different laser repetition rates, f_{rep1} = 1.9 kHz and f_{rep2} = 3.5 kHz, which resulted in irradiances P_1 = 0.27 mW/mm² and P_2 = 0.52 mW/mm². Upon photoacoustic stimulation with the lower f_{rep1}, LE RGCs showing an excitatory response had increased firing rate with the burst duration up to d_b = 25ms. Under the higher f_{rep2}, LE RGC firing rate plateaued for burst durations up to d_b = 15 ms and decreased with longer burst durations (Fig. 3A-B, left). For P23H retinae, stimulations with the lower f_{rep1} resulted in increased RGC firing rate with longer burst durations (Fig. 3A-B, right), similarly to LE rats, whereas with the higher f_{rep2}, RGC firing rate still increased for burst durations between d_b = 5 ms and d_b = 20 ms, decreasing only following longer burst durations.

LE RGC firing rates were significantly higher than for P23H RGCs for burst durations up to d_b = 25 ms and d_b = 20 ms with f_{rep1} and f_{rep2}, respectively (up to 2.8 and 4.7-fold higher, for d_b = 5 ms, and f_{rep1} and f_{rep2} , respectively, Fig. 3B). These results suggest that the degenerated retina requires higher thresholds for photoacoustic stimulation, consistent with previous findings concluding on a higher acoustic stimulation threshold in the degenerated retinae than in wild type retinae[13]. Unlike firing rate, response latencies in LE and P23H RGCs were in similar ranges and not affected by burst duration upon either f_{rep1} or f_{rep2} stimulations (Fig. 3C).

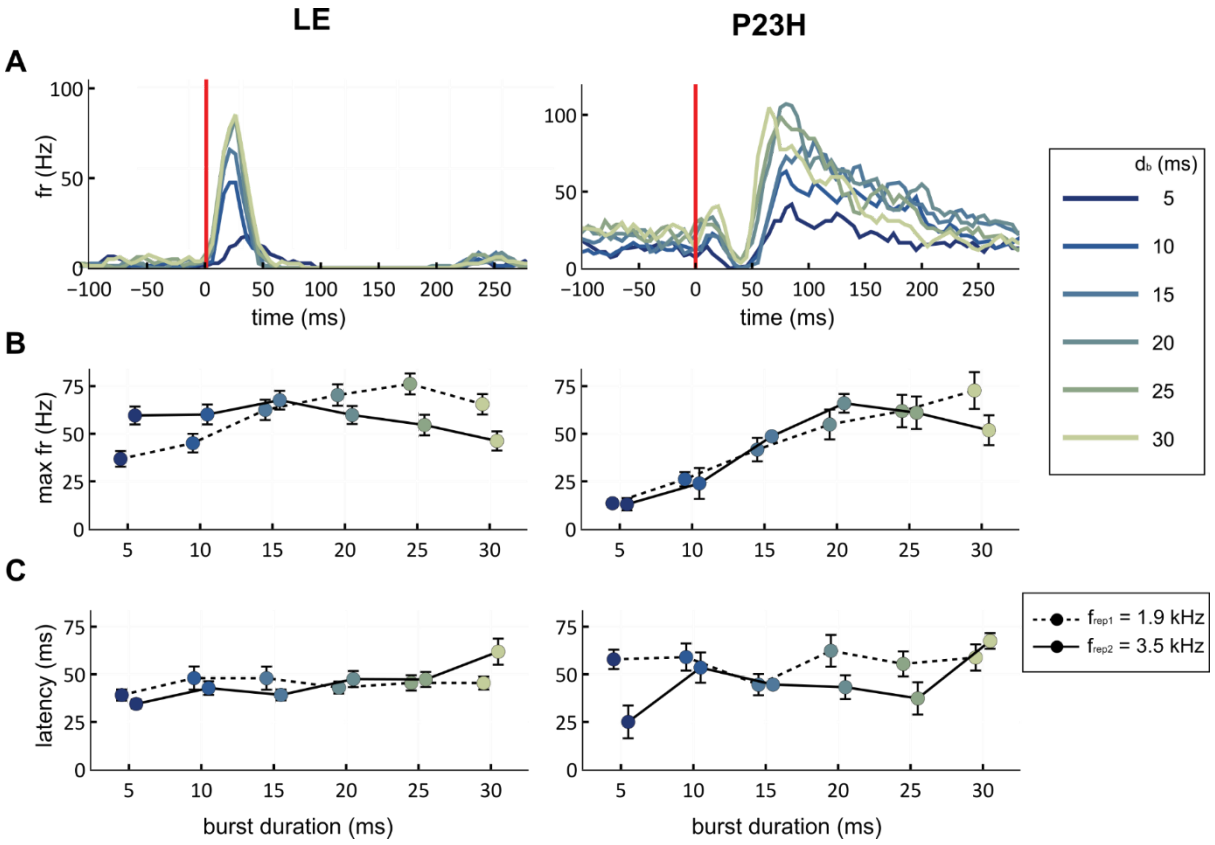

Figure 3. RGC responses under different laser burst durations and laser repetition rates. (A) Example LE (left) and P23H (right) cells displaying increased maximum firing rate (fr) with increased burst duration (recorded at f_{rep1} = 1.9 kHz). Lighter colors indicate longer burst durations (d_b= 5-30 ms). Vertical red lines: laser onset. **(B)** Maximum firing rate as a function of burst duration for LE and P23H RGCs during stimulation with repetition frequency f_{rep1} = 1.9 kHz (dashed line) and f_{rep2} = 3.5 kHz (solid line). In LE RGCs (left panel) the firing rate was positively correlated with burst duration for f_{rep1} (r = 0.91, p = 0.01, Pearson R). Data plotted as mean + SE. In P23H RGCs (right panel) firing rate was positively correlated during f_{rep1} (r = 0.996, p < 0.001) and f_{rep2} (r = 0.811, p = 0.05). With f_{rep1}, for d_b = 5 ms and 20 ms, the maximum firing rate of LE RGCs is respectively 2.8-, and 1.3-fold higher than for P23H RGCs (p < 0.001 for all conditions, Mann-Whitney U-test). With f_{rep2} , for d_b = 5 ms, the maximum firing rate of LE RGCs is 4.7-fold higher than for P23H RGCs (p < 0.001, Mann-Whitney U-test) **(C)** Response latency as a function of burst duration for LE and P23H RGCs, no significant correlation (LE: p = 0.70 and p = 0.19 for f_{rep1} and f_{rep2}, respectively; P23H: p = 0.79 and p=0.61, Pearson R). In both B and C, dashed lines: f_{rep1} = 1.9 kHz (P_1 = 0.27 W/mm^2). Solid lines: f_{rep2} = 3.5 kHz (P_2 = 0.52 W/mm^2). Dataset for B and C: for LE, n = 244 cells, recorded from 4 retinae. For P23H, n = 104 cells, recorded from 4 retinae.

Spatial resolution of *ex vivo* photoacoustic retinal stimulation

To investigate the spatial resolution of photoacoustic stimulation, we sequentially targeted multiple positions on the film by moving the fiber delivering the 1030-nm laser spot on the photoacoustic film, and mapped the activated retinal cells. Laser repetition rate was chosen at f_{rep1} = 1.9 kHz for LE and f_{rep2} = 3.5 kHz for LE and P23H retinae, respectively, to account for the higher activation threshold described above for P23H retinae. Figure 4A illustrates an example map of P23H RGCs activated after photoacoustic stimulation on 3 distinct stimulation sites during the same session. The activated RGCs were mainly located within an area slightly larger than the laser spot (< 400 µm from center). Moving the laser spot activated a different subpopulation of RGCs. To assess the spatial distribution of activated RGCs relative to the laser spot for all tested positions, we mapped the maximum RGC firing rate relative to the stimulation site (Fig. 4B). For both LE and P23H RGCs, the maximum normalized firing rate was measured under the stimulation spot. The maximum RGC firing rate was negatively correlated to the distance from the laser spot in LE and P23H retinae (Fig. 4C). Furthermore, the percentage of photoacoustic-activated RGCs decreased with the distance to the center of the laser spot (Fig. 4D). Within a 100-µm radius from the center of the 300-µm-diameter laser spot, 73% of LE RGCs and 70% of P23H RGCs showed a modified activity following the photoacoustic stimulation. This percentage decreased to 50 % of RGCs from 300 to 400 µm from the center of the laser spot for LE cells, and 200 to 300 µm away for P23H cells. These functional changes dropped to 10 % of RGCs 600 to 700 µm from the center of the laser spot for LE cells, and 300 to 400 µm away for P23H cells. These results indicate that stimulation with the PA film induces a localized response and demonstrate the possibility for a high spatial resolution of photoacoustic stimulation.

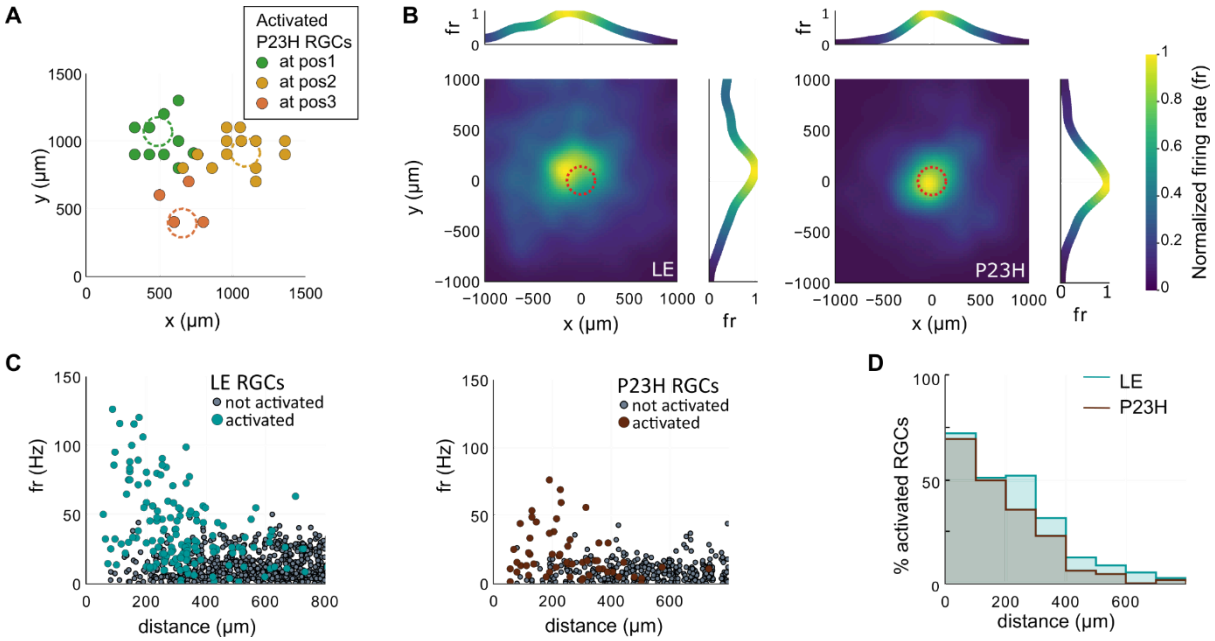

Figure 4. Spatial distribution of RGC activation upon photoacoustic stimulation. (A) RGCs were activated by moving the laser fiber along multiple sites across the film, to evaluate activation of different groups of RGCs of the same retina and the spatial distribution of activated cells. Example P23H session where the film was stimulated at three sites; cells activated at one stimulation site are grouped by color. 300-µm-diameter laser spots are marked by dashed lines. **(B)** Normalized RGC firing rate, relative to the stimulation site for LE (left, 4 retinae, 11 stimulation sites) and P23H (right, 4 retinae, 6 stimulation sites). RGC maximum firing rate was averaged between all recorded cells present at the same coordinates relative to the center of the laser spot (LE: n = 576 and P23H: n = 157 RGCs). Data was smoothed using a convolution with a 100-µm gaussian kernel. Dashed line: 300-µm-diameter laser spot. Shift between the maximum firing rate and the laser spot may be due to uncertainty on laser spot coordinates, due to 100-µm pitch of MEA used for indirect measurement of the exact laser position. **(C)** Maximum firing rate as function from distance from laser for LE (left) and P23H (right) RGCs. Stimulated firing rate is negatively correlated to distance (LE: $r = -0.310$, $p < 0.001$. P23H: $r = -0.268$, $p < 0.05$, Pearson R). Each circle is an individual cell. Cyan and brown: LE and P23H RGCs activated by photoacoustic stimulation, respectively. Gray: not activated cells. **(D)** Percentage of RGCs activated as a function of distance from the laser spot. Blue: LE cells. Brown: P23H cells. Datasets for C and D are the same as for B.

Photoacoustic implant safety in vivo

To test the feasibility of photoacoustic stimulation *in vivo*, we chronically implanted PA films in LE and P23H rats. Two designs of PA films were used for *in vivo* experiments. The PDMS/CS/PDMS film, also used in the *ex vivo* experiments, has a total thickness of 100 µm, which provides an optimal balance for low acoustic attenuation and easy handling. For the *in vivo* experiments, we also developed a uniformly mixed PDMS-CNT film (characterized in Supplementary Fig. S2). This approach allowed us to fabricate films with a total thickness of 40 µm, designed to match the 30-µm thickness of the clinically tested PRIMA photovoltaic implant, which has shown no long-term adverse effects aside from minor retinal thinning in patients[4].

To assess film safety, we subretinally implanted both PDMS/CS/PDMS and PDMS-CNT 1-mm-diameter films. After implantation, eye fundus confirmed the correct positioning of the implant near the optic nerve and general retina integrity (Fig. 5A and B). Blood vessels of the LE retina can be observed over the implant (Fig. 5A, left), indicating that the implant is in the subretinal space. Blood vessels are not visible above the implant on the P23H fundus (Fig. 5B, left), because of the difference in acquisition parameters compared to LE rats, due to the lack of pigments in the choroid of P23H rats. No complications, such as major inflammation after 7 dpi or retinal tearing, were observed on the OCT images and eye fundus.

On OCT, the average retinal thickness was 174.0 ± 2.3 µm for LE rats (n = 13) and 72.3 ± 2.3 µm for degenerated P23H rats (n = 8). At the PDMS/CS/PDMS implant position, LE retinal thickness decreased to 123.2 ± 2.9 µm at 15 dpi, 121.5 ± 4.2 µm at 30 dpi and 107.3 ± 2.0 µm at 90 dpi (Fig. 5C). In LE rats implanted with the PDMS-CNT implant, similar values of 113.0 µm ± 4.8 µm at 15 dpi and 105.8 µm at 30 dpi, were measured (Fig. 5C). The decrease in the retinal thickness above the implant in LE rats was due to photoreceptor degeneration (Fig. 5A, right), as previously reported for the PRIMA implant due to the physical separation of photoreceptors from the retinal pigment epithelium[25,26]. In implanted P23H rats, retinal thickness above the implant remained stable and comparable to the neighboring area up to four months for both PDMS-CNT and PDMS/CS/PDMS implants (Fig. 5D). These observations indicate that the photoacoustic implants have no intrinsic short-term toxicity on the wild-type and degenerated retina.

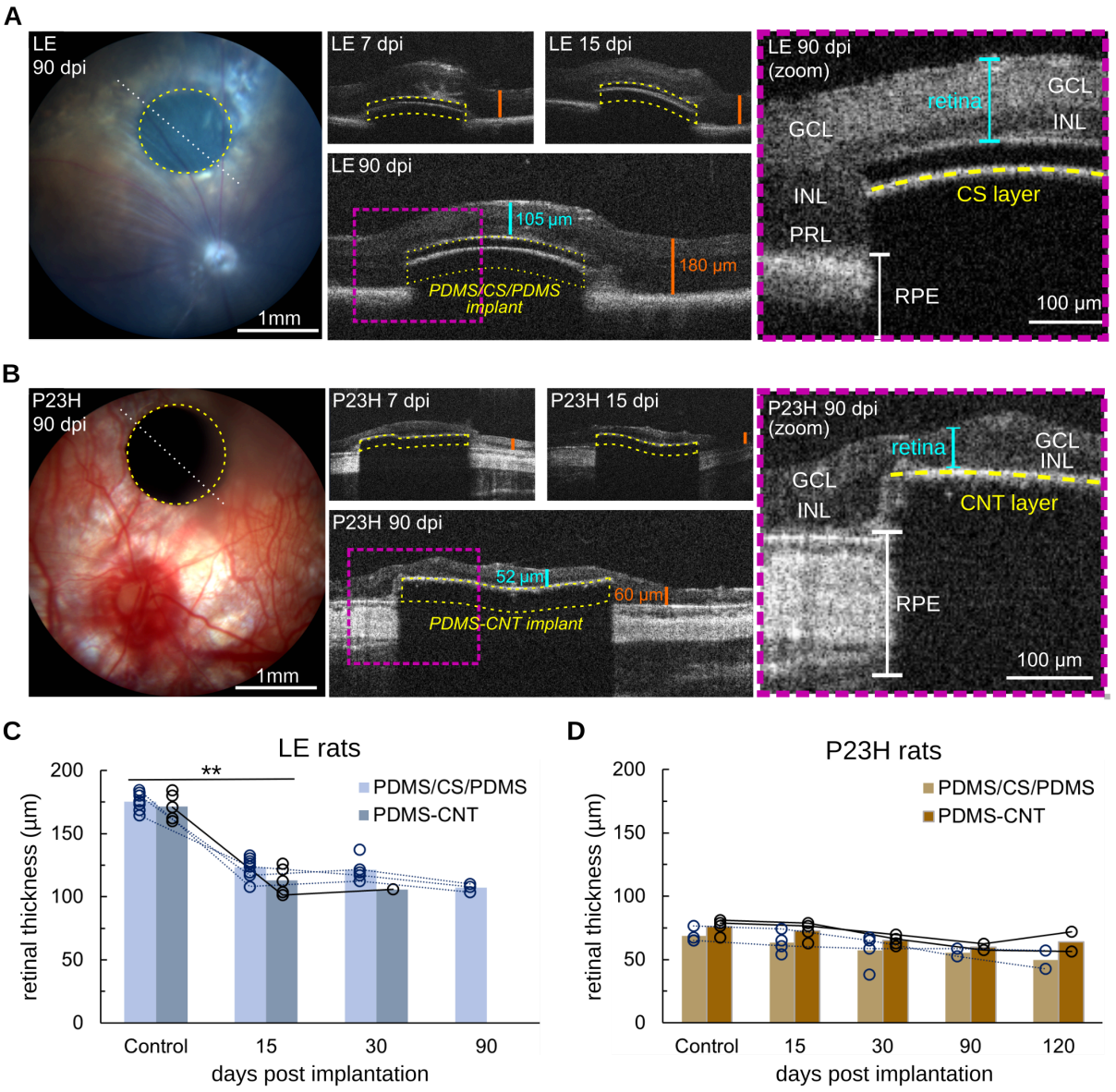

Figure 5. In vivo photoacoustic implant biocompatibility. (A) Eye fundus (left, scale bar 1 mm) and OCT (right) images of a LE rat retina with subretinal PDMS/CS/PDMS implant 7, 15, and 90 days after implantation surgery (dpi). In zoomed OCT images, GCL: retinal ganglion cell layer, INL: inner nuclear layer, PRL: photoreceptor layer. RPE: retinal pigmented epithelium. The PR layer has degenerated above the implant. Right inset: zoom on the OCT image at 90 dpi. **(B)** Same as (A) but for P23H. **(C)** Mean LE retinal thickness above PDMS/CS/PDMS (dark blue, dotted lines) and PDMS-CNT (light blue, solid lines) implants over time. Control: mean retinal thickness next to implant at 15 dpi. Thickness at 15 dpi and later is significantly lower than control thickness (**$p < 0.01$, Wilcoxon Signed-Rank test). At 15 dpi, thickness above PDMS/CS/PDMS implants is not statistically different from thickness above PDMS-CNT implants ($p = 0.16$, Mann-Whitney U test). Between 15 dpi and 90 dpi, PDMS/CS/PDMS implant thickness decrease (123.2 ± 2.9 µm to 107.3 ± 2.0) is not significant ($p = 0.25$, Wilcoxon

Signed-Rank test). **(D)** Same as (C) for P23H rats. The difference of retinal thickness above both implants is not statistically significant ($p = 0.16$ at 15 dpi and 0.32 at 30 dpi, Mann-Whitney U-test). Retinal thickness is stable up to 120 dpi for both PDMS-CNT ($p = 0.18$, one-way ANOVA) and PDMS/CS/PDMS implants ($p = 0.51$).

Photoacoustic retinal stimulation in vivo

We then examined *in vivo* photoacoustic stimulation of the degenerated retina with the subretinal photoacoustic PDMS/CS/PDMS and PDMS-CNT implants. As indicated above, photoreceptors degenerate above the implant, enabling us to define the photoacoustic activation of this blind spot in LE rats (see previous section, Fig. 5A, C). Activation of the visual pathway was assessed in the contralateral Superior Colliculus (cSC) using functional ultrasound imaging (fUS), which measures the relative changes in cerebral blood volume (rCBV) triggered by the neuronal excitation (Fig. 6A). To verify the position of the cSC, we measured its activation using control photostimulations with a full-field white light or a 595-nm laser spot. First, full-field white light stimulation of the implanted eye (P = 0.02 mW/mm²) was found to generate a large rCBV response in the cSC (Fig. 6C, a). Second, a 400-µm spot of 595-nm laser light (P = 0.21 mW/mm²) was focused onto the healthy retina next to the implant (Fig. 6B, c). It similarly triggered an increase in rCBV in the cSC (Fig. 6C, b).

We then proceeded with photoacoustic stimulation on the implant (Fig. 6B, b; Fig. 6D, top). The 1030-nm laser delivered 8 equally spaced 125 ms bursts for 2 s every 15 s, for a total of 15 stimulations per recording. These photoacoustic stimulations generated power densities P = 0.29 ± 0.06 W/mm² (mean ± SD) for PDMS/CS/PDMS implants and P = 0.39 ± 0.12 W/mm² for PDMS-CNT implant. The estimated acoustic peak-to-peak pressures at the surface of the implant were 0.11 MPa and 0.15 MPa for PDMS/CS/PDMS and PDMS-CNT implants, respectively. We observed cSC activation following the photoacoustic stimulation using both PDMS/CS/PDMS and PDMS-CNT (Fig. 6C, c, example data in Fig. 6D) implants.

To compare cSC activation by the different stimulation conditions, we averaged rCBV per rat and condition (example for single rat in Fig. 6E). The rCBV following photoacoustic stimulation significantly increased compared to the baseline measures for both PDMS/CS/PDMS and PDMS-CNT implants (Fig. 6F). Still, the rCBV responses to photoacoustic stimulations on the PDMS/CS/PDMS and PDMS-CNT implants were lower than the rCBV response following full-field white light stimulation (Fig. 6F). To control that our photoacoustic responses were not due to a mere direct infrared light stimulation of the retina, we focused the same 1030-nm laser sequence (P = 0.56 ± 0.21 W/mm², 400-µm spot) on the healthy retina next to the implant (Fig. 6C, d). No significant increase in rCBV was observed, demonstrating that the cSC activation following photoacoustic stimulation was truly caused by an acoustic mechanosensitive stimulation of the retina, and not an off-target light

stimulation. Taken together, these results show that the photoacoustic stimulation of the degenerated retina elicits a robust activation of the visual pathway downstream to the retina.

We finally compared the surfaces of the activated cSC area upon 595-nm laser stimulation and the photoacoustic stimulation, after normalizing them for each animal to the activated cSC area upon fullfield white light stimulation (Fig. 6G). Following 595-nm laser stimulation, the activated area reached 23% ± 9% (n = 6) of the area activated by the fullfield white light. Following photoacoustic stimulation, the activated area reached 42% ± 7% (n = 5) and 31% ± 11% (n = 3), with PDMS-CNT and PDMS/CS/PDMS implants, respectively. These differences between photostimulation with a 595-nm laser spot and photoacoustic stimulations with either PDMS/CS/PDMS or PDMS-CNT implants were not statistically significant. These observations demonstrate the ability of *in vivo* photoacoustic stimulation to generate a local activation of the degenerated retina, in agreement with our previous *ex vivo* observations.

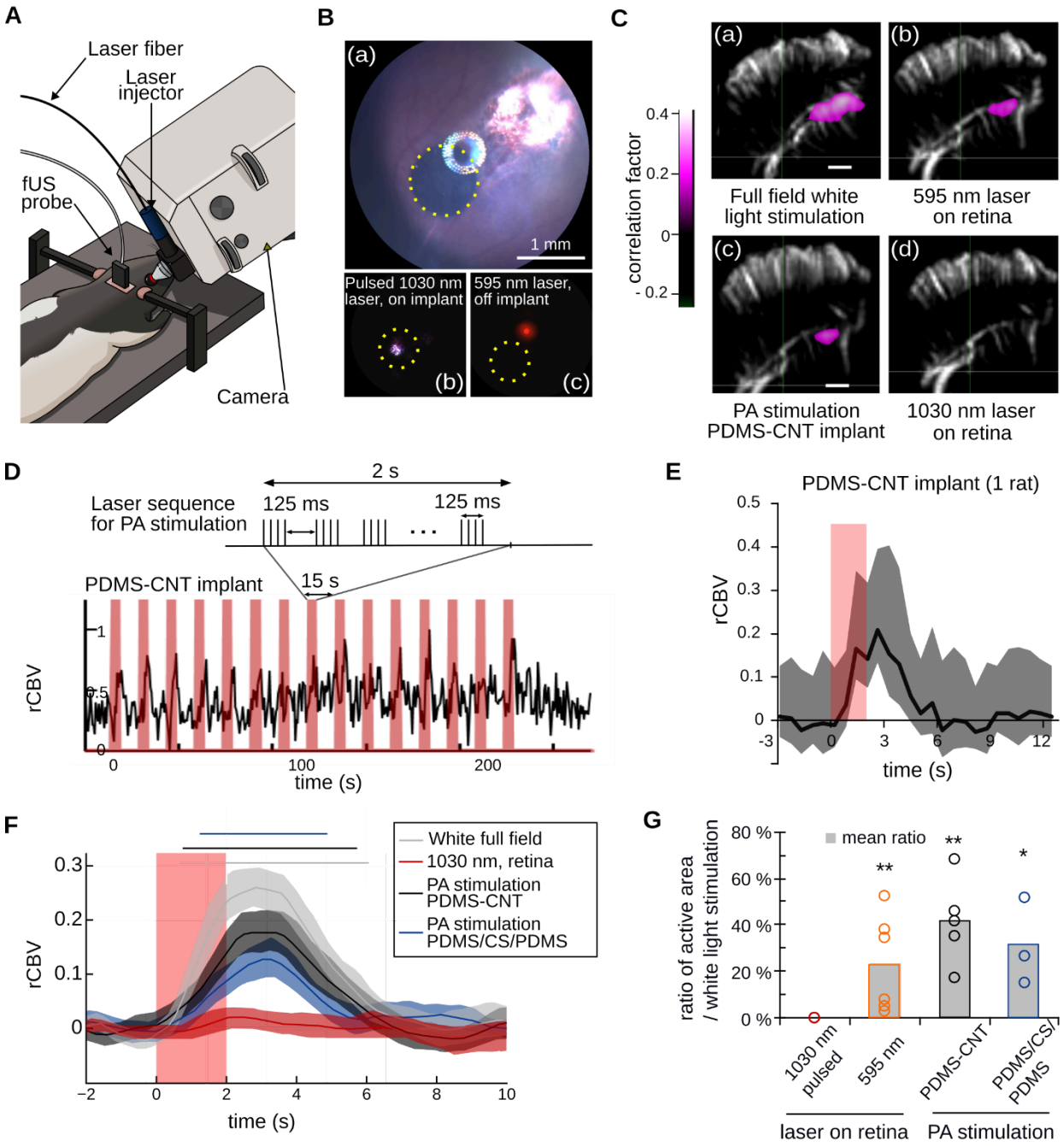

Figure 6. Superior colliculus activation following photoacoustic stimulation of in vivo LE retinae. (A) Setup for *in vivo* eye stimulation and fUS recordings. **(B)** Eye fundus images of a 1 mm PA implant (*a*) and of 400-µm laser spots (*b*: pulsed 1030-nm laser on implant, *c*: continuous 595-nm laser off implant) used for laser and photoacoustic stimulation. **(C)** Functional ultrasound imaging in the coronal plane (left hemisphere, AP Bregma, -6.5 mm). The correlation map displays the relationship between relative cerebral blood volume (rCBV) and the laser stimulation sequence. Active pixels reflect regions of activated neurons in the contralateral superior colliculus (cSC) for a single recording (15 stimulations). **(D)** Top: Laser sequence for photoacoustic stimulation (repetition rate f_{rep} = 6.1 kHz). Bottom: rCBV example trace for pulsed 1030-nm photoacoustic stimulation on a PDMS-CNT

implant (measured in 0.3 x 0.3 mm² peak correlation area of the cSC). **(E)** Average rCBV for a single session, 15 stimulations (same data as for D). Mean rCBV ± 99% CI. Laser sequence starts at 0 s. Laser is on in the red area. **(F)**. Mean rCBV responses of all individual rats following white light full field stimulation (gray, 4 rats, n = 4 recordings), 1030-nm laser stimulation on the retina (red, 3 rats, n = 4 recordings), photoacoustic stimulation using PDMS-CNT implant (black, 2 rats, n = 5 recordings) and photoacoustic stimulation using the PDMS/CS/PDMS implant (blue, 2 rats, n = 3 recordings). Horizontal bars denote significant elevation with respect to the baseline (e.g., no overlap of CI with basal CI). No significant difference in rCVB following photoacoustic stimulation between both implant types was found (e.g., overlapping confidence intervals). Peak rCBV values: white light = 0.26, PDMS-CNT = 0.18, PDMS/CS/PDMS = 0.13, 1030-nm laser on retina = 0.02. Shaded areas: 95% bootstrapped CI. **(G)** Surface ratio between the activated area following stimulation with a laser (595-nm and 1030-nm on retina and photoacoustic stimulation) and full-field white light stimulation, for all rats. The activated area is measured by counting the number of pixels on correlation maps such as (C). 595-nm laser stimulation: 3 rats, n = 6 recordings. Same data as (F) for the other conditions. Circles on the graph mark the ratio for individual recordings. Statistics: p-values vs white light stimulation: * $p < 0.05$, ** $p < 0.01$, Wilcoxon Signed-Rank test. PDMS/CS/PDMS vs 595 nm: $p = 0.71$, PDMS-CNT vs 595 nm: $p = 0.18$, PDMS/CS/PDMS vs PDMS-CNT: $p = 0.57$, Mann-Whitney U test.

Discussion

In this study, we developed flexible photoacoustic films that efficiently generated acoustic waves, which successfully stimulated retinal cells *ex vivo* and *in vivo*, thereby activating downstream visual pathways *in vivo*.

The laser wavelength and the PA materials were both optimized for safety and performance. Light wavelengths ranging from 500 nm to 1150 nm have maximum transmission in the human eye media[28]. A nanosecond laser with a 1030-nm wavelength was chosen to maximize transmission to the retina, while avoiding triggering responses in photoreceptors, as AMD patients may retain peripheral vision. CS and CNT were selected as the absorber material due their high photoacoustic conversion efficiency, accessibility, and lower safety concerns compared to lead-containing materials[29,30]. For the thermal expansion material, PDMS was identified as the best option due to its transparency, high Grüneisen parameter, excellent biocompatibility and stability[31]. The PDMS mixing ratio was adjusted to 5:1 to increase the Young's modulus, thereby enhancing photoacoustic conversion efficiency[32].

Several studies have reported the sensitivity of the retina to ultrasound stimulation[11,33,34]. Our recent study reported that photoreceptors contribute to this intrinsic ultrasound retinal sensitivity[35]. We here show that the degenerated retina maintains some ultrasound sensitivity, leading to altered RGC activity upon photoacoustic stimulation. Mechanosensitive retinal cells can also be activated *in vivo* in the degenerated retina, resulting in the activation of downstream visual pathways. It remains unclear which retinal cells apart from photoreceptors are sensitive to the ultrasound stimulation. Our results are coherent with previous studies reporting that RCGs are not directly activated by ultrasound, but that the mechanosensitivity originates upstream from RGCs in the retinal network[11,33,35]. Consistent with this conclusion, the mechanosensitive channels TRPV4 have been reported in Müller cells[23], bipolar, and ganglion cells[36]. Further studies are needed to define the cellular location of the ultrasound sensitivity in the degenerated retina and the molecular actuators generating the functional photoacoustic response.

Retinal prostheses have achieved a visual acuity in patients close to 1/20. Our photoacoustic stimulation eliminates the discrete distribution of electrodes, allowing a continuity in the retinal cell activation. High visual acuity will require spatially contained photoacoustic stimulation, which could be obtained using small laser spot sizes. In this study, a 50-µm-diameter laser spot generated an ultrasound field with a sub-100-µm resolution, a critical improvement from the 250-µm ultrasound

beam achieved in transduced based ultrasound stimulation[14]. In both wild-type and degenerated retinae, RGC activation following photoacoustic stimulation was localized around the laser spot, with a majority of RGCs activated at the laser spot. It is conceived that taking advantage of laser optics, a laser illumination of 10 µm on the implant can be achieved; therefore a sub-50-µm spatial resolution is feasible. Further studies must be performed to refine the laser spot size to further optimize biological spatial resolution.

Visual field, like visual acuity, is a critical component of vision. Visual field size required for efficient navigation is around 20 degrees[37], which can be achieved with an implant wider than 5 mm. D. Ghezzi has argued that greater visual field (~45°) could allow for significantly restored patient autonomy even with poor visual acuity (< 1/20)[37]. Retinal prostheses currently implanted in humans are rigid and therefore constrained to diameters below 3 mm. Unlike those, the flexible PDMS-based PA films can conform to the curvature of the eye and can be folded for implantation, which makes them suitable for larger (> 5 mm) subretinal implants.

A pressure of 0.11 MPa was found to be sufficient to elicit responses in the superior colliculus with the PDMS/CS/PDMS film. This is an order of magnitude lower than the pressure threshold of 1.7 MPa at 20 MHz reported by Lu and colleagues[14] for their non-invasive acoustic stimulator and below the activation pressures obtained by Cadoni and colleagues[35] (0.2 to 1.27 MPa at 15 MHz) for sonogenetics. Our approach thus greatly decreased the US pressure required for the stimulation of the retina. Pressure threshold of the photoacoustic stimulation based on both films correspond to a mechanical index value MI < 0.10 (PDMS-CNT film) and 0.06 (PDMS/CS/PDMS film) and spatial peak temporal average Intensity I_{SPTA} < 0.94 and 0.25 mW/cm^2, respectively, meeting FDA safety thresholds for ultrasonic ophthalmic devices[38] of MI < 0.23 and I_{SPTA} < 50 mW/cm² (see Supplementary Table T1). Moreover, these FDA safety guidelines set the maximum local temperature increase to 1 °C. Temperature increases with the photoacoustic stimulation parameters used *ex vivo* and *in vivo* have been measured to be below 1 °C at the film surface. No transient temperature events faster than the 2 kHz acquisition frequency are expected to occur (Supplementary Fig. S7).

For vision restoration applications such as an artificial retina, it is necessary to project an image through patterned illumination. As temperature increase is cumulative, the 1 °C FDA-mandated threshold may be exceeded due to multiplexing. Strategies can be deployed to minimize the overall laser energy required to transmit visual information, such as light pattern optimization (Supplementary Fig. S8). In addition to safe stimulation, we have shown promising results regarding the biosafety of the photoacoustic implants. No major adverse effects on the healthy or degenerate implanted retina were detected over a 4 month period. Unlike electrostimulation, the presence of

glial cells between the implant and the retina would not substantially affect stimulation efficacy as acoustic attenuation is below 10 dB/mm[39]. Further histology studies must be done to precisely assess eventual implant-driven cell death.

While further studies are required to investigate the mechanisms of photoacoustic retinal stimulation and whether the implant can restore meaningful vision to patients afflicted by retinal degenerative diseases, our results collectively demonstrate that photoacoustic retinal stimulation through flexible implants opens up potential for a innovative strategy for restoring vision, with high precision and a large field of view.

Material and methods

Fabrication of the photoacoustic films

To fabricate 100-µm-thick PDMS/CS/PDMS film, a uniform layer of candle soot was flame-synthesized and deposited onto a glass slide for 20 s, achieving a thickness of approximately 3 µm. Subsequently, a degassed PDMS mixture of silicone elastomer base and curing agent (Sylgard 184, Dow Corning Corporation, USA) with mix ratios of 5:1 was spin-coated at 500 rpm onto the candle soot layer, and cured at 110 °C for 15 minutes. The resulting cured film was then detached from the glass slide, inverted, and reattached. Another layer of PDMS mixture was spin-coated at 500 rpm and cured at 110 °C for 15 minutes. Both sides of the film were treated for 1 min with oxygen plasma to make the implant surface hydrophilic[41]. The film was cut into smaller areas (5 x 5 cm^2) and stored in distilled water before use to avoid reversion to their hydrophobic state. 1 mm and 1.5 mm biopsy punches (Kaimedical) were used to make individual photoacoustic films for *ex vivo* and *in vivo* experiments.

To fabricate a 40-µm-thick 15%wt CNT-PDMS film, we employed a recipe derived from previous work[16]. We initially prepared PDMS at mix ratios of 10:1. Subsequently, a 15%wt of CNT (<8 nm OD, 2–5 nm ID, length 0.5–2 µm, VWR, Inc., USA) was mixed with the PDMS, aided by the addition of IPA to facilitate CNT dissolution. The resulting mixture underwent a 5-minute sonication process, followed by a 30-minute degassing step to eliminate bubbles and IPA. The prepared mixture was then spin-coated onto a glass substrate at 500 rpm for 5 minutes. The coated substrate was cured at 110 °C for 15 minutes.

Characterization of photoacoustic properties of films

The photoacoustic properties of films were characterized with a 40-µm needle hydrophone system (NH0040, Precision Acoustics Inc., UK) or an 85-µm needle hydrophone system (HGL-0085, Onda Corporation, USA). For illumination, a Q-switched diode-pumped laser with a pulse width of 8 ns (RPMC, wavelength 1030 nm, repetition frequency 2.9 kHz, USA) was delivered to one side of the film via a multimode fiber with a 200-µm core (FT200UMT, Thorlabs, USA). On the other side of the film, the hydrophone was mounted on a 3D stage and aligned with the illuminated area by the optical fiber. The signals were amplified with a pulser-receiver (Olympus, Model 5073PR, USA) and then recorded via a digital oscilloscope (Rigol, DS4024, USA).

Mapping the photoacoustic pressure field

Photoacoustic field microscopy was used to map the generated ultrasound field, as previously reported[42]. Here a 1064-nm pulsed laser (OPOLETTE 355 LD, OPOTEK, pulse duration 5 ns) was used

as the pump beam. A continuous wave 1310-nm laser (1310LD-4-0-0, AeroDIODE Corporation) serves as the probe. A piece of PDMS/CS/PDMS film was mounted on a 50-µm optical fiber (FG050UGA, Thorlabs) and the 1064-nm laser was delivered to the film sample to generate the photoacoustic signals. A translation stage (ProScan III, Prior) was used to scan the generated ultrasound field. Under a single ns pulse, the PA-induced refractive index change was detected as the imaging contrast.

Temperature measurements

A J-type thermocouple with a 200-µm tip was set against the PDMS/CS/PDMS film inside 3% agarose gel, typically used for mimicking tissue[43]. The PDMS/CS/PDMS film was attached to a 200-µm optical fiber to assure the alignment between the illuminated area on the film and the thermocouple tip. A Q-switched diode-pumped laser with a pulse width of 4.5 ns (RPMC, wavelength 1030 nm, USA) was used to illuminate the film. The temperature rise on the film was recorded with a 2 kHz sampling rate from 10 recordings. Average data was computed from the 3 recordings with the highest temperature rise. Photos of the setup are shown in Supplementary Fig. S9.

Animals

All animal experiments were conducted at the Vision Institute Paris, in accordance with the National Institutes of Health Guide for the Care and Use of Laboratory animals. Protocols were approved by the Local Animal Ethics Committee (Committee Charles Darwin CEEACD/N°5, project reference Apafis#40263-2023010909277429 v5) and conducted in agreement with Directive 2010/63/EU of the European Parliament. Wild-type Long-Evans male rats aged between 2 and 8 months were obtained from Janvier Laboratories. P23H male and female transgenic rats (9-14 months old) were raised locally. P23H rats serve as a model for autosomal dominant retinitis pigmentosa[44].

Ex vivo experiments

Ex vivo retina preparation and blockers

The following procedures were carried out under dim red light. Animals were dark adapted for 30 minutes, then anesthetized with CO2 and euthanized by cervical dislocation. The eyes were enucleated and hemisected in carboxygenated (95% O2, 5% CO2) RINGER medium containing (in mM): 125 NaCl, 2.5 KCl, 1 $MgCl_2$, 1.25 NaH_2PO_4, 20 glucose, 26 $NaHCO_3$, 1 $CaCl_2$ and 0.5 L-Glutamine at pH 7.4. The medium was continuously perfused in the recording chamber at a speed of 1.5 mL/min and was kept around 37 °C.

Isolated retinae were placed on a dialysis membrane (Spectra/Por® 6 50 kD dialysis membrane, Spectrum) coated with poly-L-lysine (0.1%, Sigma), with the photoacoustic film between the dialysis membrane and the retina, and with photoreceptors against the film. The retinae were pressed against an MEA (MEA256 iR-ITO; Multi-Channel Systems, Reutlingen, Germany) with a custom 3D-printed piece.

AMPA/kainate glutamate receptor antagonist 6-cyano-7-nitroquinoxaline-2,3-dione (CNQX, 20 µM, Tocris Bioscience) and NMDA glutamate receptor antagonist (RS)-3-(2-carboxypiperazin-4-yl)-propyl-1-phosphonic acid ((RS)-CPP, 10 µM, Tocris Bioscience) were bath applied through the perfusion line.

Ex vivo photoacoustic retinal stimulation

Photoacoustic stimulations were done with a 1030-nm, 4.2-ns-pulsed laser (One DPSS, Bright Solutions) delivered through a 200-µm-core SMA/SMA fiber (Thorlabs Inc, USA., ref M25L01). A second 200-µm-core was connected to the first fiber using a fixed attenuator (Thorlabs Inc., USA, ref FA26M) to control the power density. The optical fiber was inserted into a custom 3D-printed holder incorporated in a motorized XYZ stage with 0.5-nm precision (Sensapex, uMp-3 micromanipulator). It was lowered above the PA film at a ~90° angle. A low power 650-nm guiding beam (FIBERCHECK, Laser Components) was used to map the beam position. The laser illumination spot size was measured in ImageJ using MEA electrode pitch as reference.

Laser pulse repetition rate and the laser burst trains were controlled using a Teensy microcontroller custom written software (C++, Java, Python). In a typical stimulation, the laser delivered 10 µJ pulses with a repetition frequency f_{rep} of 1.9 kHz or 3.5 kHz during a single 5-ms to 30-ms burst, repeated at

1 Hz for 40 bursts. PA film integrity was confirmed by the lack of photoelectric effect in the MEA recordings (Supplementary Fig. S4).

Analysis of MEA recordings

MEA raw traces were recorded through the MEA software (MC Rack, Multichannel Systems). Spikes were sorted using SpyKING CIRCUS [45], and manually curated using phy[46]. Spikes were referenced relative to stimulus onset and grouped across trials in bins using a sliding window (bin width = 20 ms, increments = 5 ms). Cell activity in each bin was estimated using bootstrap resampling (n = 1000 resamples, 99% confidence intervals), and considered significantly increased or decreased if there were no overlapping confidence intervals compared to baseline (200 - 100 ms before stimulus onset).

RGCs were considered responsive or activated if their firing rate was significantly increased or decreased compared to baseline for at least 15 ms consecutively, and response latency was defined as the first bin of this series. Noise clusters were filtered from the cell clusters by excluding cells with response latencies below 5 ms. A 300-µm diameter area was illuminated by the 1030-nm laser (200-µm fiber) during photoacoustic stimulation. For quantifying responsive cells and dose responses (Fig. 2 and 3) we included only cells within 300-µm of the center of the illuminated area ("stimulation site"). Cells with a response latency above 250 ms were excluded, as they were likely not a result from direct stimulation.

To analyze the relation between cell activation and distance from the stimulation area (Fig. 5A), we assigned the firing rate of each cluster to a bin in a grid with a spacing of 25 µm, and convolved it with a gaussian kernel (sigma = 100 µm).

In vivo experiments

Successful implantation was defined as good positioning of the 1mm film in the subretinal space, and no occurrence of complications due to surgery. N = 8 adult (9-10 mo) P23H rats were successfully implanted and used for biocompatibility studies. N = 7 adult Long-Evans rats were successfully implanted at 8 weeks of age and used for photoacoustic stimulation.

Surgery procedures for chronic subretinal implantation

A 1-mm-diameter PA film was surgically placed in the subretinal space in the central region next to the optic nerve, as previously described[47]. Briefly, a small sclerotomy was performed on the dorsal sclera tangential to the cornea. A gel of sodium chondroitin sulfate – sodium hyaluronate (Viscoat Alcon) was injected in the sclerotomy to generate a retinal detachment. The implant was then inserted below the detached retina in the subretinal space, targeting an adjacent location to the optic disk.

Ocular imaging

Eye fundus imaging (MICRON® IV, Phoenix, USA) and optical coherence tomography (Bioptigen® OCT system, Leica microsystems, Germany) data were collected at 7 and 15 days post-implantation (dpi) for all rats to monitor inflammation state and correct implantation, and at 30, 60, 90 and 120 dpi for rats that did not undergo prior retinal stimulation.

Cranial window acute surgery

Anesthesia was provided with an intraperitoneal injection of 40 mg/kg ketamine (Axience, France) and 0.14 mg/kg medetomidine (Domitor®, Vétoquinol, France) diluted in sodium chloride. The animal was placed on a stereotaxic frame to perform a left craniotomy. Drops of ocular gel (Lubrithal®, Dechra, France) were applied and the eyes were then covered with a black cloth for dark adaptation. A rectangular piece of bone was removed from Bregma -3 mm to -8 mm.

Retinal stimulation and brain imaging

Retinal stimulation was performed 26 - 40 days after implantation surgery for rats implanted with PDMS/CS/ODMS implants and 23 - 29 days after implantation surgery for PDMS-CNT implants, and immediately after the cranial window surgery. The rats were re-injected with anesthesia every 45 min with one-third of the initial dose, up to a maximum of 5 injections. The animals were euthanized at the end of the experiment using an intracardiac injection (Exagon®, Axience, France).

For full field light stimulations with a white LED source, light power on the retina was estimated to be ~0.02 mW/mm² based on the power entering the pupil, P_{pupil} = 1.2 mW. The choice of the stimulation protocol was informed by prior retina studies using fUS[48,49]. Each 1.8 s stimulation sequence was made of 6 evenly spaced 300 ms illuminations (LED on), repeated 15 times.

For 595-nm, 1030-nm laser stimulation and photoacoustic stimulation, focused laser spots were aimed using a laser Injector from the MICRON 810-nm Image-Guided Laser modality combined with a MICRON® III camera (Phoenix, USA). A low power 650-nm guiding beam (FIBERCHECK, Laser Components) was coupled to the injector to safely choose the area to stimulate. The rat's implanted eye was covered in ocular gel (Lubrithal®, Dechra, France) and in contact with the camera lens. Stimulation sequences for all 3 modalities were identical.

For 595-nm (continuous) laser stimulation, power density on retina was 26 µW in a 400 ± 26 -µm-diameter laser spot. For photoacoustic stimulation, the same 1030-nm pulsed laser as for the *ex vivo* experiments was used. Laser energy exiting the laser injector was E_p = 15 µJ/pulse. To aim at the implant for photoacoustic stimulation, the laser focal spot was not placed on the optical axis of the injector lens, which resulted in a loss of power. All the laser diameter at $1/e^2$ (D_L) and laser power density P were estimated from average intensity profiles extracted with Fiji/ImageJ (Supplementary Fig. S11 and S12) and are expressed as the mean ± standard deviation.

For 1030-nm laser stimulation on the retina: D_L = 470 ± 70 µm. P = 0.56 ± 0.21 W/mm²,
for 1030-nm photoacoustic stimulation with PDMS-CNT implants: D_L = 360 ± 60 µm. P = 0.39 ± 0.12 W/mm²,
for 1030-nm photoacoustic stimulation with PDMS/CS/PDMS implants: D_L = 410 ± 45 µm. P = 0.29 ± 0.06 W/mm².

For PDMS/CS/PDMS implants, 3 recordings (n = 2 rats) were obtained with the fUS probe at Bregma -6.5 mm and 4 recordings (n = 3 rats) at Bregma -6 mm. For PDMS-CNT implants, 5 recordings (n = 2 rats) were obtained with the fUS probe at Bregma -6.5 mm and 4 recordings (n = 2 rats) at Bregma -6 mm. Results on recordings at Bregma -6 mm are presented in Supplementary Fig. S6. The laser beam was moved on a different area of the implant after each recording.

Changes in Cerebral Blood Volume (CBV) were measured with a system dedicated to small animal ultrasound neuroimaging (Iconeus, Paris, France). Ultrasonic gel was applied on the dura. The ultrasonic probe was lowered and placed ~1 mm above the dura, ensuring complete immersion in

the ultrasound gel. The probe was positioned coronally at Bregma -6 mm, - 6.5 mm and -7 mm in order to measure CBV in the contralateral superior colliculus.

The pupil of the eye of interest was dilated with a tropicamide-based eye drop solution (Mydriaticum®, Théa, France) before the first recording. The body temperature was monitored with a rectal probe and maintained using a heating blanket. Respiratory and heart rates were continuously monitored (TCMT, Minerve, France). After local application of lidocaine (4 mg/kg, Laocaïne ®, MSD, France), the thinned skull was exposed and covered with ultrasound gel. The rats were scanned with a system dedicated to small animal ultrasound neuroimaging (Iconeus, Paris, France). Doppler vascular images were obtained using the Ultrafast Compound Doppler Imaging technique[50]. Each frame was a compound plane wave frame[51] resulting from the coherent summation of backscattered echoes obtained after successive tilted plane waves emissions. Then, the blood volume signal was extracted from the tissue signal by filtering the image stacks with a dedicated spatiotemporal filter using Singular Value Decomposition[52]. Each transcranial Power Doppler image was obtained from 200 compounded frames acquired at 500 Hz frame rate.

Analysis of in vivo experiments

Analysis of OCT images

Mean retinal thickness next to the implant and above the implant were measured with ImageJ on OCT images (diametral slices). The number of rats imaged 30 days post-implantation (dpi) and later was lower than the number imaged at 7 dpi and 15 dpi because rats were used for terminal retinal stimulation recordings starting at 23 dpi.

Analysis of functional ultrasound imaging recordings

The correlation map of the CBV variations and the laser sequence for stimulation was computed by the manufacturer's proprietary IcoStudio software. A 3 s delay was computed in the calculation of the correlation to account for vascular delay. In correlation map displays (Fig 6C), only significant pixels with a correlation threshold greater than 0.2 appear. Relative CBV variations (rCBV) in a 300 x 300 µm² region of interest (ROI) centered on the peak intensity of the correlation map were extracted. For each recording (15 laser stimulations), the cerebral blood flow (CBV) was normalized into a relative steady-state value (rCBV) and calculated as the following: $rCBV = (CBV(t) - CBV_0)/CBV_0$, with CBV(t) the power doppler value t seconds after the start of laser sequence and CBV_0 the

baseline in the ROI. The baseline was defined as the mean power doppler value 5 seconds before the start of the laser sequence. The data was bootstrapped to calculate confidence intervals.

Statistical analysis

Values are expressed and represented as mean values ± standard error of the mean (SE) on figures and in the text, unless specified otherwise. Similarly, in scatter plots with error bars (Fig 1, Fig 3), data points and error bars represent the mean and the standard error of the mean, respectively.

Statistical significance was analyzed with Wilcoxon signed-rank tests and Mann-Whitney U tests (Fig. 2 to 6). Pearson correlation (Fig. 2 to 4) was computed to quantify the strength and direction of the linear relationship between two continuous variables. One-way ANOVA was used to test the effect of a single factor on the mean of a dependent variable (Fig 5). Finally, to estimate confidence intervals for a statistic of unknown distribution (average rCBV variations in Fig. 6) we used bootstrapped estimation (1000 samples, 95% confidence intervals). Statistical tests are provided in the figure legends.

Acknowledgements

This work was supported by the BRAIN Initiative R01 NS109794 to J-XC and CY, BRAIN/NEI R21 EY035437 to CY by National Institute of Health, United States, by the Foundation Fighting Blindness (PPA-0922-0840-INSERM and PPA-0922-0840-INSERM) to SP, by IHU FOReSIGHT, France, (ANR-18-IAHU-01) to SP, by the European Research Council (Grant Agreement 101045289) to SP, and by Axorus SAS, France, to SP and CY.

Competing interests

This study was funded in part by the company Axorus SAS. J-DL and HM are major stakeholders in Axorus. CY and J-XC are minor stakeholders in Axorus.

References

1. Jeany Q Li *et al.* Prevalence and incidence of age-related macular degeneration in Europe: a systematic review and meta-analysis. *Br. J. Ophthalmol.* **104**, 1077 (2020).

2. Da Cruz, L. *et al.* Five-Year Safety and Performance Results from the Argus II Retinal Prosthesis System Clinical Trial. *Ophthalmology* **123**, 2248–2254 (2016).

3. Wu, K. Y., Mina, M., Sahyoun, J.-Y., Kalevar, A. & Tran, S. D. Retinal Prostheses: Engineering and Clinical Perspectives for Vision Restoration. *Sensors* **23**, 5782 (2023).

4. Muqit, Mmk. *et al.* Prosthetic Visual Acuity with the PRIMA System in Patients with Atrophic Age-related Macular Degeneration at 4 years follow-up. Preprint at https://doi.org/10.1101/2023.11.12.23298227 (2023).

5. Reutsky-Gefen, I. *et al.* Holographic optogenetic stimulation of patterned neuronal activity for vision restoration. *Nat. Commun.* **4**, 1509 (2013).

6. Sahel, J.-A. *et al.* Partial recovery of visual function in a blind patient after optogenetic therapy. *Nat. Med.* **27**, 1223–1229 (2021).

7. McGregor, J. E. *et al.* Optogenetic restoration of retinal ganglion cell activity in the living primate. *Nat. Commun.* **11**, 1703 (2020).

8. Gauvain, G. *et al.* Optogenetic therapy: high spatiotemporal resolution and pattern discrimination compatible with vision restoration in non-human primates. *Commun. Biol.* **4**, 125 (2021).

9. Chaffiol, A. *et al.* A New Promoter Allows Optogenetic Vision Restoration with Enhanced Sensitivity in Macaque Retina. *Mol. Ther.* **25**, 2546–2560 (2017).

10. Shen, Y., Campbell, R. E., Côté, D. C. & Paquet, M.-E. Challenges for Therapeutic Applications of Opsin-Based Optogenetic Tools in Humans. *Front. Neural Circuits* **14**, 41 (2020).

11. Menz, M. D., Oralkan, Ö., Khuri-Yakub, P. T. & Baccus, S. A. Precise Neural Stimulation in the Retina Using Focused Ultrasound. *J. Neurosci.* **33**, 4550–4560 (2013).

12. Gong, C. *et al.* Non-Invasive Hybrid Ultrasound Stimulation of Visual Cortex In Vivo. *Bioengineering* **10**, 577 (2023).

13. Qian, X. *et al.* Noninvasive Ultrasound Retinal Stimulation for Vision Restoration at High Spatiotemporal Resolution. *BME Front.* **2022**, 9829316 (2022).

14. Lu, G. *et al.* Noninvasive imaging-guided ultrasonic neurostimulation with arbitrary 2D patterns and its application for high-quality vision restoration. *Nat. Commun.* **15**, 4481 (2024).

15. Ali, Z., Zakian, C. & Ntziachristos, V. Ultra-broadband axicon transducer for optoacoustic endoscopy. *Sci. Rep.* **11**, 1654 (2021).

16. Shi, L. *et al.* Non-genetic photoacoustic stimulation of single neurons by a tapered fiber optoacoustic emitter. *Light Sci. Appl.* **10**, 143 (2021).

17. Du, Z. *et al.* Photoacoustic: A Versatile Nongenetic Method for High-Precision Neuromodulation. *Acc. Chem. Res.* **57**, 1595–1607 (2024).

18. Zheng, N. *et al.* Photoacoustic Carbon Nanotubes Embedded Silk Scaffolds for Neural Stimulation and Regeneration. *ACS Nano* **16**, 2292–2305 (2022).

19. Lee, H. C. *et al.* Histological evaluation of flexible neural implants; flexibility limit for reducing the tissue response? *J. Neural Eng.* **14**, 036026 (2017).

20. Andersen, M. A. & Schouenborg, J. Polydimethylsiloxane as a more biocompatible alternative to glass in optogenetics. *Sci. Rep.* **13**, 16090 (2023).

21. Chen, G. *et al.* High-precision neural stimulation by a highly efficient candle soot fiber optoacoustic emitter. *Front. Neurosci.* **16**, 1005810 (2022).

22. Menz, M. D. *et al.* Radiation Force as a Physical Mechanism for Ultrasonic Neurostimulation of the *Ex Vivo* Retina. *J. Neurosci.* **39**, 6251–6264 (2019).

23. Zhuo, S.-Y. *et al.* Mechanism of low-frequency, low-intensity ultrasound modulation of the mouse retina. *J. Neural Eng.* **20**, 036025 (2023).

24. Chen, G. *et al.* High-precision photoacoustic neural modulation uses a non-thermal mechanism. Preprint at https://doi.org/10.1101/2024.02.14.580331 (2024).

25. Lorach, H. *et al.* Development of Animal Models of Local Retinal Degeneration. *Investig. Opthalmology Vis. Sci.* **56**, 4644 (2015).

26. Prévot, P.-H. *et al.* Behavioural responses to a photovoltaic subretinal prosthesis implanted in non-human primates. *Nat. Biomed. Eng.* **4**, 172–180 (2019).

27. Prévost, F., Lepore, F. & Guillemot, J.-P. Spatio-temporal receptive field properties of cells in the rat superior colliculus. *Brain Res.* **1142**, 80–91 (2007).

28. Van Den Berg, T. J. T. P. & Spekreijse, H. Near infrared light absorption in the human eye media. *Vision Res.* **37**, 249–253 (1997).

29. Li, Y. *et al.* Optically-generated focused ultrasound for noninvasive brain stimulation with ultrahigh precision. *Light Sci. Appl.* **11**, 321 (2022).

30. Du, X. *et al.* Lead halide perovskite for efficient optoacoustic conversion and application toward high-resolution ultrasound imaging. *Nat. Commun.* **12**, 3348 (2021).

31. Noimark, S. *et al.* Polydimethylsiloxane Composites for Optical Ultrasound Generation and Multimodality Imaging. *Adv. Funct. Mater.* **28**, 1704919 (2018).

32. Qiang, Z., Zhang, Y., Groff, J. A., Cavicchi, K. A. & Vogt, B. D. A generalized method for alignment of block copolymer films: solvent vapor annealing with soft shear. *Soft Matter* **10**, 6068–6076 (2014).

33. Jiang, Q. *et al.* Temporal Neuromodulation of Retinal Ganglion Cells by Low-Frequency Focused Ultrasound Stimulation. *IEEE Trans. Neural Syst. Rehabil. Eng.* **26**, 969–976 (2018).

34. Naor, O., Hertzberg, Y., Zemel, E., Kimmel, E. & Shoham, S. Towards multifocal ultrasonic neural stimulation II: design considerations for an acoustic retinal prosthesis. *J. Neural Eng.* **9**, 026006 (2012).

35. Cadoni, S. *et al.* Ectopic expression of a mechanosensitive channel confers spatiotemporal resolution to ultrasound stimulations of neurons for visual restoration. *Nat. Nanotechnol.* **18**, 667–676 (2023).

36. Gao, F., Yang, Z., Jacoby, R. A., Wu, S. M. & Pang, J.-J. The expression and function of TRPV4 channels in primate retinal ganglion cells and bipolar cells. *Cell Death Dis.* **10**, 364 (2019).

37. Ghezzi, D. The role of the visual field size in artificial vision. *J. Neural Eng.* **20**, 023001 (2023).

38. FDA. Marketing Clearance of Diagnostic Ultrasound Systems and Transducers - Guidance for Industry and Food and Drug Administration Staff. (2023).

39. Rabell-Montiel, A., Anderson, T., Pye, S. D. & Moran, C. M. Attenuation Coefficients of the Individual Components of the International Electrotechnical Commission Agar Tissue-Mimicking Material. *Ultrasound Med. Biol.* **44**, 2371–2378 (2018).

40. Rabell-Montiel, A., Thomson, A. J., Anderson, T. A., Pye, S. D. & Moran, C. M. Acoustic Properties of Small Animal Soft Tissue in the Frequency Range 12–32 MHz. *Ultrasound Med. Biol.* **44**, 702–713 (2018).

41. Duangkanya, K., Kopwitthaya, A., Chanhorm, S. & Infahsaeng, Y. Oxygen plasma treatment time induced hydrophilicity of polydimethylsiloxane (PDMS) thin films for liquid lenses application. *Mater. Today Proc.* **65**, 2442–2445 (2022).

42. Cheng, J.-X. *et al.* Millimeter-deep micron-resolution vibrational imaging by shortwave infrared photothermal microscopy. *Res. Sq.* rs.3.rs-3449548 (2023) doi:10.21203/rs.3.rs-3449548/v1.

43. Chen, P. *et al.* Acoustic characterization of tissue-mimicking materials for ultrasound perfusion imaging research. *Ultrasound Med. Biol.* **48**, 124–142 (2022).

44. Orhan, E. *et al.* Genotypic and Phenotypic Characterization of P23H Line 1 Rat Model. *PLOS ONE* **10**, e0127319 (2015).

45. Yger, P. *et al.* A spike sorting toolbox for up to thousands of electrodes validated with ground truth recordings in vitro and in vivo. *eLife* **7**, e34518.

46. Rossant, C. *et al.* Spike sorting for large, dense electrode arrays. *Nat. Neurosci.* **19**, 634–641 (2016).

47. Salzmann, J. Subretinal electrode implantation in the P23H rat for chronic stimulations. *Br. J. Ophthalmol.* **90**, 1183–1187 (2006).

48. Provansal, M. *et al.* Functional ultrasound imaging of the spreading activity following optogenetic stimulation of the rat visual cortex. *Sci. Rep.* **11**, 12603 (2021).

49. Morisset, C. *et al.* Retinal functional ultrasound imaging (rfUS) for assessing neurovascular alterations: a pilot study on a rat model of dementia. *Sci. Rep.* **12**, 19515 (2022).

50. Bercoff, J. *et al.* Ultrafast compound doppler imaging: providing full blood flow characterization. *IEEE Trans. Ultrason. Ferroelectr. Freq. Control* **58**, 134–147 (2011).

51. Montaldo, G., Tanter, M., Bercoff, J., Benech, N. & Fink, M. Coherent plane-wave compounding for very high frame rate ultrasonography and transient elastography. *IEEE Trans. Ultrason. Ferroelectr. Freq. Control* **56**, 489–506 (2009).

52. Demene, C. *et al.* Spatiotemporal Clutter Filtering of Ultrafast Ultrasound Data Highly Increases Doppler and fUltrasound Sensitivity. *IEEE Trans. Med. Imaging* **34**, 2271–2285 (2015).

Supplementary Information for

A flexible high-precision photoacoustic retinal prosthesis

Audrey Leong[†1], Yueming Li[†2], Thijs R. Ruikes[†1], Julien Voillot[3], Yuhao Yuan[1], Guo Chen[1], Arnaud Facon[3], Chakrya-Anna Chhuon[3], Corentin Joffrois[1], Gilles Tessier[1], Marion Cornebois[1], Julie Dégardin[1], Jean-Damien Louise[3], Ji-Xin Cheng[2*], Chen Yang[2*], Hélène Moulet[3#*], Serge Picaud[3#*].

† equal contribution, [#] equal contribution

[1] *Institut de la Vision, Sorbonne Université, INSERM, CNRS, Paris, 75012, France*

[2] *Department of Electrical and Computer Engineering, Boston University, Boston, MA, 02215, USA*

[3] *Axorus SAS, Loos, 59120, France*

**Corresponding authors: helene.moulet@axorus.com, cheyang@bu.edu, serge.picaud@inserm.fr,*

1 Properties of the photoacoustic films

1.1 Young's Modulus of PDMS/CS/PDMS photoacoustic film

We measured the Young's Modulus E of the PDMS/CS/PDMS film using a tensile test (Supplementary Fig. 1) and the equation below:

$$E = \frac{Stress}{Strain} = \frac{FL}{A\Delta L}$$

Following our measurements, we estimated the PDMS film's Young's modulus between 0.5-5 GPa. The PDMS film's Young's modulus is orders of magnitude lower than silicon-based implants (200-300 GPa), but remains orders of magnitude higher than the retina's Young's modulus, estimated between 0.5 kPa[3] and 25 kPa[4].

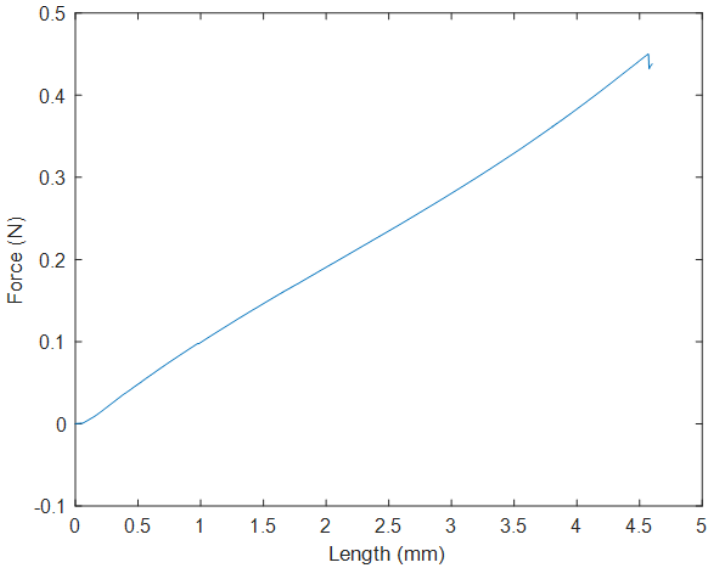

Supplementary Figure S1. Raw data from the tensile test to calculate Young's Modulus. A piece of PDMS/CS/PDMS film was cut into rectangular for the tensile test and stretched while measuring the deformation and the required force.

1.2 Peak pressure and energy conversion efficiency of the PDMS/CS/PDMS film

Hydrophone measurements (NH0040, Precision Acoustics Inc., UK) 900 μm away from the PDMS/CS/PDMS film measured a peak pressure 146.2 kPa when stimulated with a 1030 nm laser delivering 8 ns pulses with an energy of 7 μJ per pulse, resulting in a normalized peak pressure P_{peak} = 21 kPa/μJ . We sought to estimate P_{peak0} , the peak pressure at the surface of the photoacoustic (PA) film.

With a 50 µm fiber pressure decay PDMS/CS/PDMS between 0 and 700 µm is a factor 3.0 (Fig 1D. in main text), with a slope that decreases with distance. 700 µm from the PA film surface, peak pressure is only 1.3-fold smaller than at 400 µm. We therefore estimate P_{peak0} to be approximately 3 x higher than the pressure 900 µm from the surface. P_{peak} was measured following photoactivation with a 200 µm laser fiber. Pressure decay is expected to be slower for larger illumination areas. As we intend to use P_{peak0} to assess compliance to FDA safety thresholds (Section 4), we prefer to overestimate the real value. Peak pressure at the surface of the PDMS/CS/PDMS film is therefore estimated to be $P_{peak0} = P_{peak} \times 3 = 63$ kPa/µJ.

The conversion efficiency is then derived using:

$$E_{CE} = E_A / E_O$$

Where E_O is the optical energy (energy per pulse, $E_O = 10\,\mu J$) and E_A the acoustic energy given by:

$$E_A = \frac{A}{\rho c} \int_0^\infty p^2(t) dt$$

With A the area of the 200 µm diameter laser spot, ρ the density of water (998 kg/m^3), c the speed of sound (1480 m/s), and p the peak-to-peak pressure of the acoustic wave (P_{peak0}).

Given our estimated peak pressure P_{peak0} = 63 kPA/µJ, we find an energy conversion efficiency value of $E_{CE} = 3.0 \times 10^{-4}$ % when applying a surface energy of 32 mJ/cm² (E = 10 µJ per pulse).

1.3 Characterization of PDMS-CNT film for in vivo photoacoustic retinal stimulation

We developed a second type of photoacoustic (PA) film for the in vivo experiments: a 40 µm thick PDMS-CNT film (Supplementary Fig. S2A). As for the PDMS/CS/PDMS film, photoacoustic signals were generated by delivering a pulsed laser at 1030 nm and recorded with a hydrophone set 0.9 mm away from the film. The PDMS-CNT film emitted ultrasound with a peak pressure 133 kPa for a laser energy of 10 µJ per pulse, resulting in P_{peak}= 13.3 kPa/µJ. The PDMS/CNT film provides a central frequency at 10.9 MHz (vs 42.2 MHz for the PDMS/CS/PDMS film) and -6 dB bandwidth of 5.9 to 15.8 MHz (Supplementary Fig. S2B).

Prior results by Chen and colleagues reported a decay factor of 5[1], which was used to estimate the peak pressure P_{peak0} at the surface of the PDMS-CNT film. This resulted in $P_{peak0} = P_{peak} \times 5 = 66$ kPa/µJ and an energy conversion efficiency $E_{CE} = 8.3 \times 10^{-4}$ % for a surface energy of 32 mJ/cm² (E=10 µJ/pulse).

In vivo in rats and humans, the distance between the inner retina and the PA implant will be below 100 µm[2]. In the inner retina, the peak pressures of the acoustic waves generated with the PDMS-CNT and PDMS/CS/PDMS implants are therefore not expected to differ significantly (less than a factor 2).

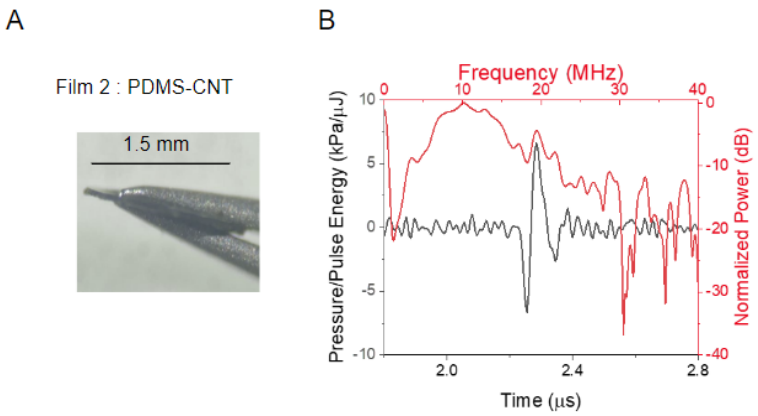

Supplementary Figure S2. Characterization of the PDMS-CNT photoacoustic film. **(A)** CNT-embedded PDMS with a thickness of 40 µm. **(B)** PA performance in the temporal domain (black) and frequency domain (red) of the photoacoustic films corresponding to films shown in A.

2 Optical properties of the PDMS/CS/PDMS film

2.1 Optical properties of the CS layer

To control for direct activation of photoreceptors by 1030 nm laser stimulation when the laser fiber is placed above the PA film, we measured the transmittance of the CS layer. The absorbance of a candle soot layer deposited on glass through flame deposition (same protocol as for PDMS/CS/PDMS fabrication) was measured with a spectrophotometer (UV-1900i from Shimadzu). At 1030 nm, transmission T_1 = 0.53 % for a L_1=1 µm thick CS layer (Supplementary Fig. S3).

In the PDMS/CS/PDMS implants, the CS layer is 3 µm thick. According to Beer-Lambert law law, expected light transmission T(L) at 1030 nm for a L=3 µm thick layer is: $T(L) = exp(-(1-T_1) * L/L_1$, we therefore find T (L) = 1.5 10^{-5} %.

Adsorption of the CS in the PDMS may affect how compact the layer is and increase transmittance compared to the theoretically expected values.

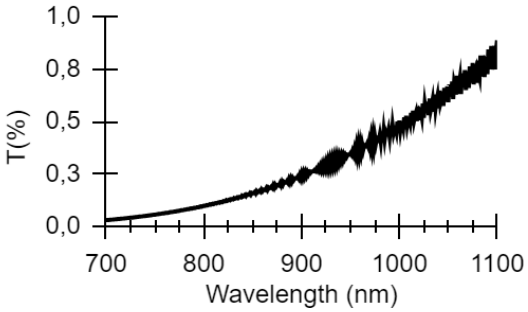

Supplementary Figure S3. Transmittance (T) of a 1 µm thick CS layer.

2.2 Laser absorption by the photoacoustic film

In this study, we use a multi-electrode array (MEA) to measure retinal ganglion cell activity. We therefore characterized the film against an MEA chip as a control and indirectly characterized light transmission by the PDMS/CS/PDMS film. Similarly to ex vivo experiments, the film was immersed in the RINGER solution. Following photo activation of the PA film, a low frequency electrical signal is measured by the MEA at the onset of photoacoustic stimulation (Supplementary Fig. S5A). The amplitude and the kinetics of the signal are dependent on the laser parameters and are coherent with an indirect measurement of local changes to temperature. When the 1030 nm pulsed laser directly illuminates the MEA (Supplementary Fig. S5 B, C, D), it generates a strong photoelectric signal, with individual voltage peaks for each laser pulse. At comparable energy density, the photoelectric signal is much stronger than the slow wave signal generated by the PA film. The lack of photovoltaic effect when the MEA is covered by the PA film is coherent with the expected low light transmission of the film.

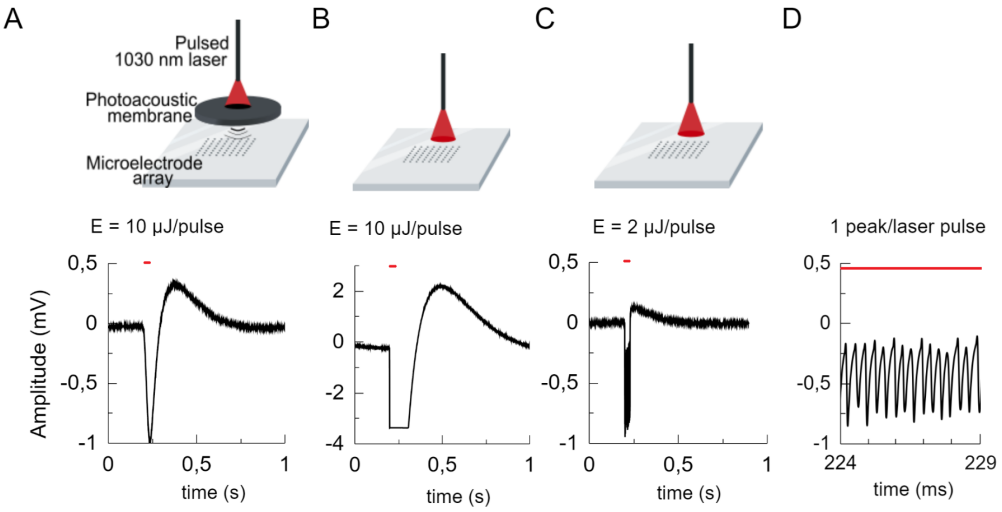

Supplementary Figure S4. Raw voltage recording on the MEA electrode closest to the center of the laser beam with and without PDMS/CS/PDMS implant. **(A)** Top : setup with PA film between laser and MEA. Bottom : voltage recording from the MEA electrode on which the laser is centered (greatest signal amplitude on MEA). Red horizontal line : laser ON. Laser protocol is a single 30 ms pulsed 1030 nm laser burst with a repetition rate f_{rep} = 2.94 kHz. Energy per pulse E=10 µJ. **(B)** Top : setup with laser directly illuminating the MEA. Bottom : same as A. Laser protocol : burst duration d_b=30 ms. E= 10 µJ per pulse (identical to A). MEA saturation for voltage signals > 3.4 µV. **(C)** Same setup as B. Laser protocol : d_b=15 ms. E= 2 µJ per pulse. E divided by 5 and d_b divided by 2 to avoid MEA saturation and obtain voltage signals of comparable amplitude to A. **(D)** Magnified version of the X axis of plot C.

3 Superior colliculus activation following photoacoustic retinal stimulation (PARS) of in vivo LE retinae.

3.1 Population data for 595 nm light retinal stimulation

Only pixels with a correlation threshold between the laser (or full field white light) stimulus sequence and the relative cerebral blood volume variations (rCBV) increase greater than 0.2 are displayed on the correlation map in Figure 6C of the main text. For lower correlation values, the increase of rCBV compared to the baseline is not significant. Supplementary Fig.S6A shows additional correlation maps (bottom line) with a 0.1 minimum pixel correlation threshold. With this lowered threshold, pixels appear in the contralateral Superior Colliculus (cSC) of the brain for 1030 nm laser stimulation of the retina. This suggests that for higher laser energy levels, the cSC may significantly respond to infrared pulsed stimulation.

Supplementary Fig. S5B displays the same data as Fig. 5F in the main text, with added data (orange curve) for 595 nm laser stimulation on the retina. The diameter of the laser spot used for 595 nm laser stimulation and PARS are quite similar (~ 400 µm).

Peak rCBV values: white light = 0.26 (reached 2.84 s after the start of the laser sequence), 595 nm = 0.24 (2.01 s), PDMS-CNT = 0.18 (3.28 s), PDMS/CS/PDMS = 0.13 (3.15 s), 1030 nm laser on retina = 0.02 (2.20 s). At this stage, we do not know how those differences in rCBV correlate with visual perception, nor can we infer on the quality of visual perception following PARS.

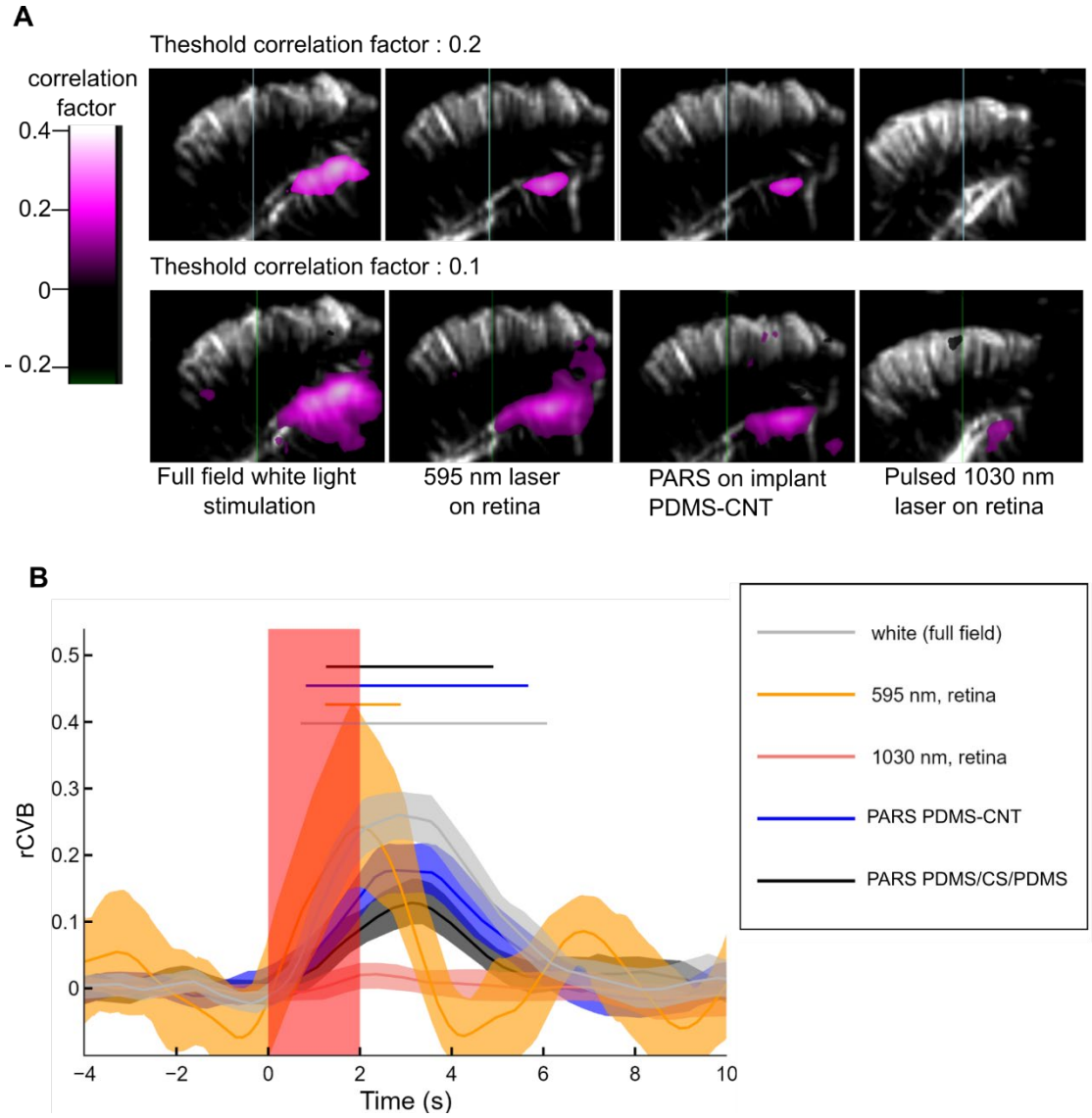

Supplementary Figure S5. Superior colliculus activation following PARS of in vivo LE retinae. **(A)** Brain slice of one rat (coronal plane, left hemisphere, AP Bregma -6.5 mm) with correlation maps displaying cSC activation for a single recording (15 stimulations). Top line: threshold for pixel display of activation is a 0.2 correlation between rCBV and the laser sequence (same as Fig. 6C in the main text). Bottom line: threshold is 0.1. Activation other than in the cSC, and activation areas non contiguous with the larger area, appear. **(B)** Average of the mean rCBV values in the 0.3 x 0.3 mm² peak correlation area of the superior colliculus of all individual rats. Shaded areas: 95% bootstrapped CI. Horizontal bars denote significant elevation with respect to the baseline (no overlap of CI with basal CI). White light stimulation: 4 rats; 595 nm: 3 rats, n = 6 recordings; 1030 nm laser stimulation on the retina: 3 rats, n = 4; PARS with PDMS-CNT: 2 rats, and n = 5; PARS with PDMS/CS/PDMS: 2 rats, n = 3.

3.2 Impact of fUS probe position on measured rCBV

The rCVB response curve following 595 nm laser stimulation on the retina is consistent between multiple recording positions along the antero-posterior axis (-6, -6.5 and -7 mm relative to Bregma, Supplementary Fig. 6A). However, when recording the rCVB at those positions during PARS with either the PDMS/CS/PDMS or PDMS-CNT implant, the response seems flattened over time (Supplementary Fig. 6C and D). This may suggest differences in stimulation spatial resolution in the cSC between laser and PARS. This may also suggest that the difference in delay between the start of the laser sequence and peak rCBV (previous section, Supplementary Fig. S5) for PARS (~ 3 s) compared to 595 nm stimulation (~ 2 s) may be due to nonoptimal positioning of the recording probe during PARS.

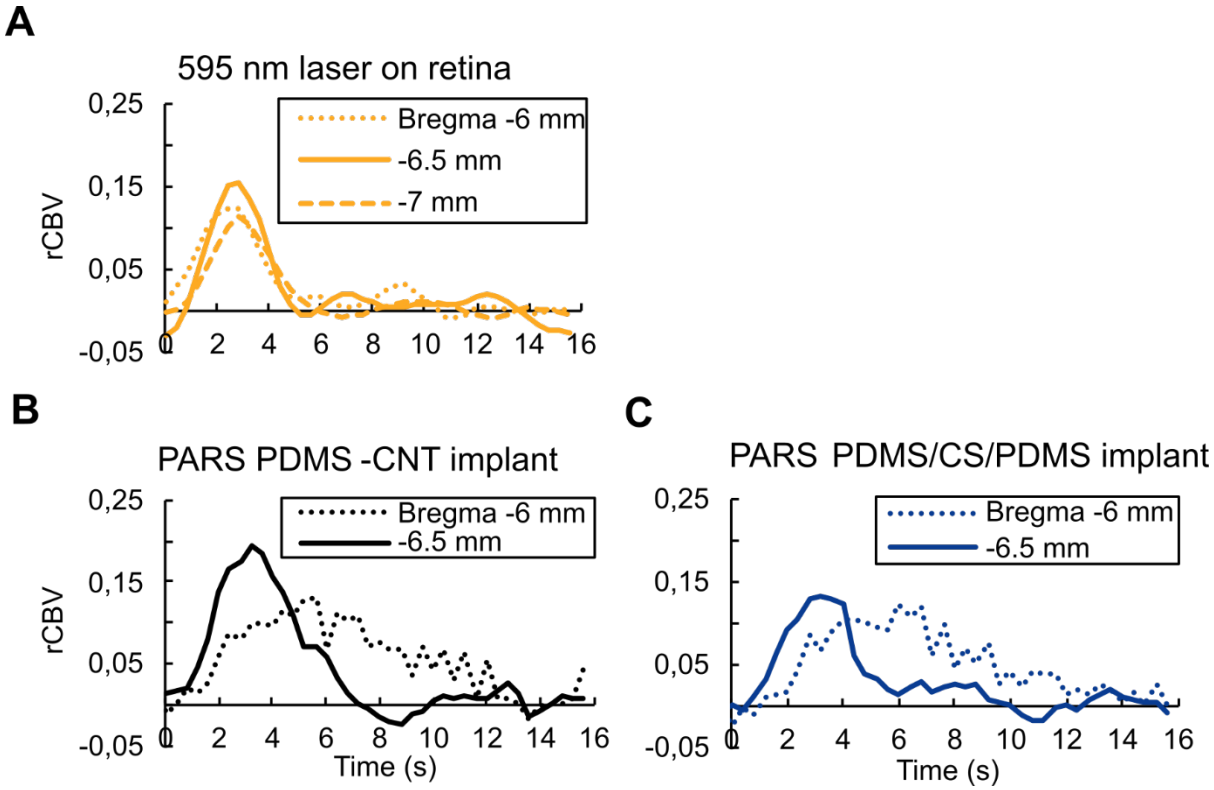

Supplementary Figure S6. rCBV recordings along the antero-posterior axis **(A)** Average rCBV following 595 nm laser stimulation of the retina. 1 rat, n= 1 laser position. **(B)** Same as A for PARS with PDMS-CNT implants. 2 rats, n= 4 positions. **(C)** Same as A for PARS with PDMS/CS/PDMS implants. 3 rats, n=4 positions.

4 Safety considerations : FDA thresholds

4.1 Mechanical index and spatial peak temporal average ultrasonic Intensity

FDA safety regulations for ophthalmic devices (https://www.fda.gov/media/71100/download) prescribe a mechanical index (MI) < 0.23, and spatial peak temporal average ultrasonic Intensity (I_{SPTA}) < 50 mW/cm². These are defined as follows :

- MI = NPP / √f, with NPP the negative peak pulse (acoustic) pressure in MPa and f the acoustic frequency in MHz.

- I_{SPTA} = I * f_{rep} / f * dc, with f_{rep} the laser repetition frequency, f the acoustic frequency and dc the duty cycle (total stimulation duration divided by 1 second) and I (W/cm²) the ultrasound intensity of a single pulse. I = $\int_0^\infty p^2(t)dt$ / ρc , with ρ the density of water, c the speed of sound, and p the peak-to-peak pressure of the acoustic wave.

To calculate I_{SPTA}, we assumed the maximum value for dc, i.e. dc = 1 (constant stimulation).

First, in order to obtain upper bound values for MI and I_{SPTA}, MI and I_{SPTA} were calculated considering the laser parameters which result in the strongest optical stimulation. Specifically, those used for PARS ex vivo : laser energy is E=10 µJ per pulse delivered by a 200 µm-diameter fiber with a repetition frequency of 3.5 kHz. NPP and peak-to-peak pressure values at the surface of the film are estimated from the experimentally measured energy conversion efficiency, as per Section 1.

Note that to establish these upper bound values, we consider that the laser spot diameter on the film during PARS is identical to that used for establishing the energy conversion efficiency of the PA film (~ d_0 = 200 µm). In practice, the laser spot in ex vivo studies was closer to d_1 = 300 µm in diameter (mean laser energy density P = 0.52 W/mm²). At constant laser energy per pulse, both NPP and p are expected to decrease as laser spot diameter increases. For a rough estimate, we could consider that NPP and p values are linearly correlated to laser energy density, and so are to be divided by $(d_1 / d_0)^2$ = 2.25 to be closer to the expected experimental values.

For both PA films, MI and I_{SPTA} obtained are below FDA thresholds (Supplementary Table T1, green lines). MI and I_{SPTA} values for the PDMS/CS/PDMS film are lower (a factor 3 and a factor 17, respectively) than that of the PDMS-CNT film, making it the safer option.

Second, we estimated lower bound values for MI and I_{SPTA} (gray lines).

In vivo, mean laser spot size was 360 µm for PARS with the PDMS-CNT implant (mean laser energy density P = 0.39 W/mm²) and 410 µm (P = 0.29 W/mm²) for PARS with the PDMS/CS/PDMS implant. Using the laser parameters for in vivo PARS and assuming that NPP and p values are linearly correlated with laser energy density, we can calculate lower bound values for MI and I_{SPTA}. The lower bound values are 4 to 6-fold lower than the upper bound values.

PA film	Laser spot diameter (µm)	f (MHz)	NPP (MPa)	**MI**	I (mW/cm²)	**I_{SPTA} (mW/cm²)**
PDMS-CNT	200 (ex vivo)	10.9	0.33	**0.10**	2924	**0.94**
	360 (in vivo)	10.9	0.07	**0.02**	447	**0.25**
PDMS/CS/PDMS	200 (ex vivo)	42.2	0.42	**0.06**	2624	**0.22**
	410 (in vivo)	42.2	0.07	**0.01**	307	**0.04**

Supplementary Table T1. **Ultrasound characterization of photoacoustic films.** NPP: negative peak pressure, MI: mechanical index, I: ultrasound intensity, I_{SPTA}: spatial peak temporal average intensity. Green lines : upper bound values calculated using the laser parameters for ex vivo PARS and assuming a 200 µm laser spot diameter. Gray lines : lower bound values calculated using the laser parameters for in vivo PARS. The listed values comply with FDA thresholds for mechanical index (MI) and average acoustic intensity (I_{SPTA}) : MI < 0.23 and I_{SPTA} < 50 mW/cm².

4.2 Temperature increase

FDA safety guidelines for ophthalmic devices (https://www.fda.gov/media/71100/download) set the maximum local temperature increase to 1°C. Temperature increases with the laser stimulation parameters used *ex vivo* (Fig. 1G) and *in vivo* (Supplementary Fig. S8) have been measured to be below 1°C at the film surface with a thermocouple.

No transient temperature events faster than the thermocouple 2 kHz acquisition frequency are expected to occur considering the laser repetition frequencies used in this study, which are between 1.9 kHz and 6.1 kHz.

The thermocouple's acquisition frequency (2 kHz) cannot capture transient temperature events in the 0.1-1 ms range, which have been reported to activate heat-sensitive TRPV1 channels in cases of very high (> 15 K) temperature increases[5]. Such transient peaks would have to be induced by the individual laser pulses. This is incompatible with the absorber-to-cell distances in our system. The transient component of the temperature rise induced by laser pulses with a repetition frequency f_{rep} propagates over a distance driven by the thermal diffusion length $\mu = \sqrt{(D/f_{rep})}$, where D is the thermal diffusivity of the medium. If we consider $D_{water} \approx 0.14$ mm²/s (Diffusivity is in the range of 0.1 - 0.2 mm²/s for both pure[6] and carbon-loaded PDMS) and a repetition frequency of 3.7 kHz, then the thermal diffusion length is μ = 6.2 µm. In the PDMS/CS/PDMS implants, the minimum distance of cells to the CS layer is 50 µm. Therefore, we do not expect transient temperature events to activate heat-sensitive channels.

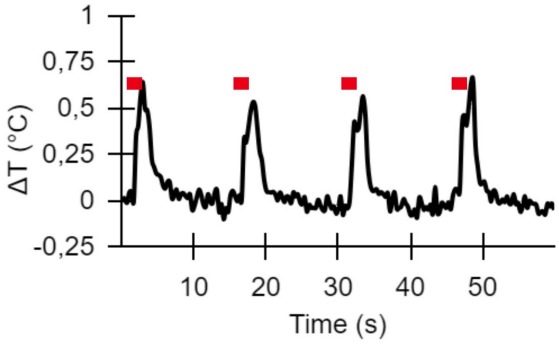

Supplementary Figure S7. **Temperature increase during in vivo stimulation conditions.** Temperature increase (ΔT) at the membrane surface during 1030 nm laser irradiation. P = 0.34 W/mm². Red lines : laser ON. Same stimulus paradigm as for implant stimulation in vivo. Maximum temperature increase (ΔT) of 0.84 °C.

4.3 Other safety concerns

In the retina and, more generally, the eye, plasma formation due to high energy laser pulses is a concern. Peak laser power in this study, defined as surfacic pulse energy divided by pulse duration, is P_{peak} ~ 10^5 W/mm². This value is orders of magnitude below the threshold for plasma formation on the cornea, lens and retina (P_{peak} ~ 10^8 W/mm² for 6 ns laser pulses[7].

4. Strategies to improve thermal safety

4.1 Pattern optimization

Thermal increase generated by a single laser spot was under 1°C. For vision restoration applications such as artificial retinas, stimulation with patterned laser spots is necessary to recreate complex images. Temperature increase is cumulative, so mitigating strategies should be used to comply with the 1°C FDA mandated threshold.

One such strategy involves projecting only the edges of an image on the implant to keep the subject of the image recognizable for the patient while reducing the overall required laser energy by a factor ten. In Supplementary. Fig. S8, the displayed face requires only 6 % of the laser energy that would be required to illuminate the whole area. To draw such a pattern of light with a 50 µm laser spot, the total implant would have to be ~ 5 x 5 mm² which is approximately the size of the human macula.

Supplementary Figure S8: **Projecting the edges of an image is a strategy to reduce laser power density.** 100 x 100 pixels binary image of a face. The white pixels fill 6 % of the total area.

4.2 Laser source optimisation

Additionally, laser wavelength could be further optimized for safety. Tissue absorption at 1030 nm is on the high side for in vivo experiments (~50% total transmission to the retina, versus ~ 95 % at 532 nm[8]. In the NIR spectrum, suitable laser sources exist at 1064 nm, for which transmission is ~ 65%. Since most AMD patients retain living photoreceptors (rods) and parafoveal residual perception, additional tests on laser safety will also be required to evaluate potential photochemical damage.

5 Extended Methods

5.1 Thermocouple measurements with setup

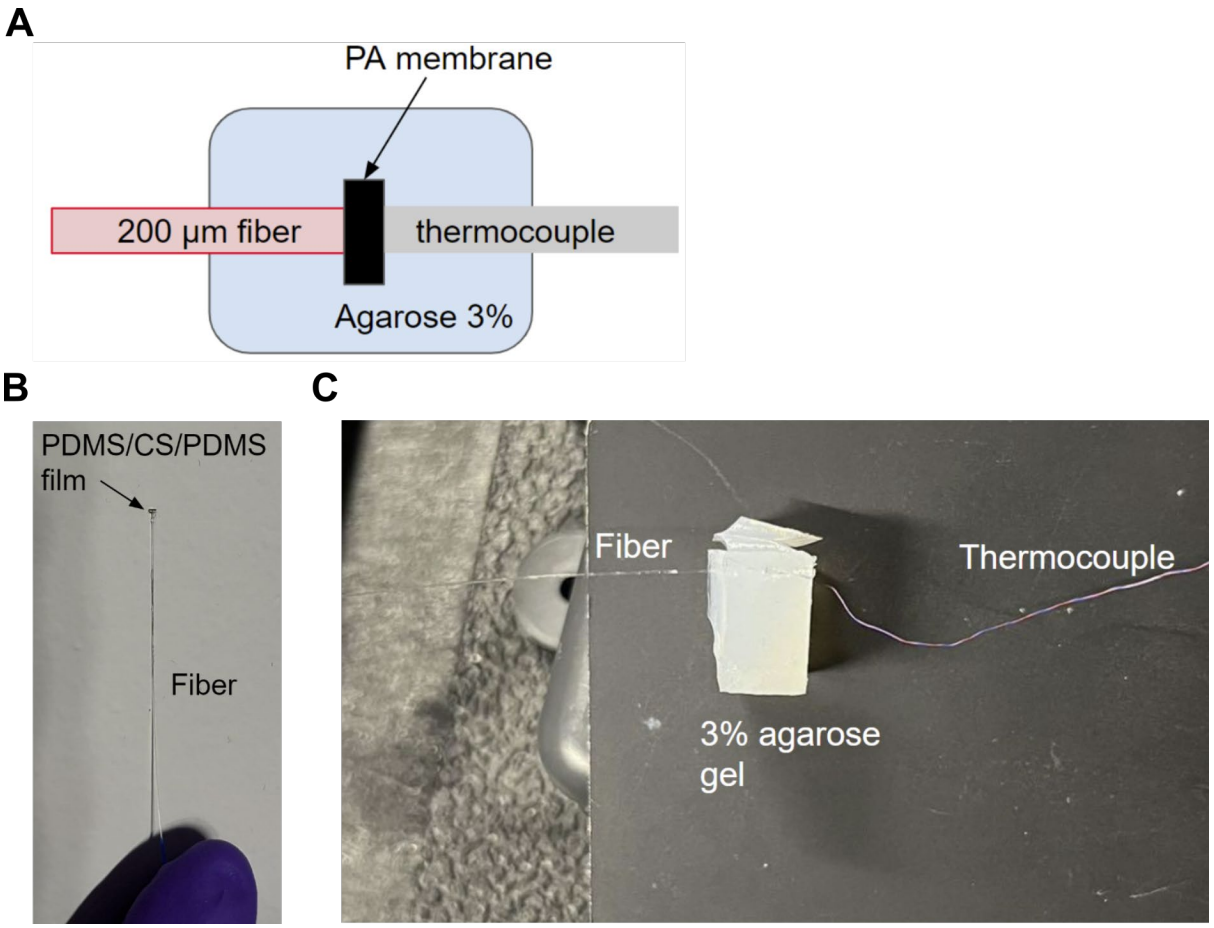

Supplementary Figure S9. **Thermocouple measurement setup photos. (A)** Schematic of the setup. **(B)** Small PDMS/CS/PDMS film placed on the tip of a 200 µm optical fiber to facilitate alignment with the 200 µm thermocouple. **(C)** Aligned fiber, PA film and thermocouple sensor in 3% agarose gel.

5.2 Ex vivo: RGC count per stimulation site

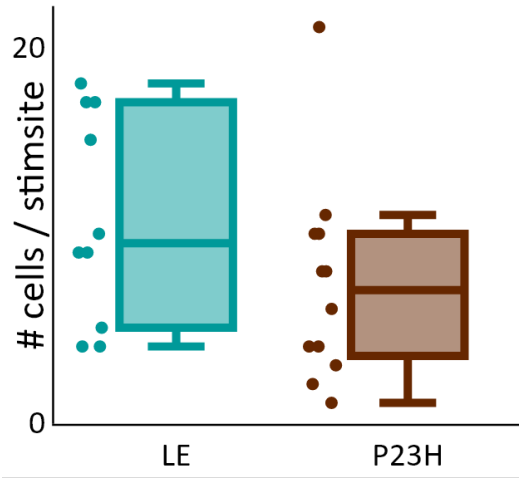

Supplementary Figure S10. **RGC cell count per stimulation site.** **(A)** Average number of RGCs with baseline activity in a 600 µm diameter area (the "stimulation area") centered on the 300 µm diameter area illuminated by the laser during stimulation. Each dot represents an individual stimulation area. LE: 10 stimulation areas from 4 retinas, n = 11 ± 5 cells per stimulation area (mean ± S.D.). P23H: 12 stimulation areas from 5 retinas, n = 7 ± 5 cells per stimulation area.

5.3 In vivo - laser irradiance calculation

Characterizing laser beam exiting the laser injector (no eye)

The laser Injector from the MICRON 810 nm Image-Guided Laser modality is designed to project a laser spot of similar size to the diameter of the optical fiber used for delivery at the focal point of the injector lens. At the focal plane (7 mm from the injector lens, equivalent to the average diameter of a rat's eye) the measured laser beam radius upon delivery with a 200 µm diameter fiber was w_1 = 162 µm.

Continuous laser stimulation with a repetition frequency f_{rep}= 6.1 kHz was applied into the laser injector. The power exiting the laser injector (P_0 in W) was measured with a power meter. The resulting energy per pulse E_{p0} was calculated using $E_{p0} = P_0 / f_{rep}$. E_{p0} = 15 µJ/pulse.

When the laser beam goes out of the injector on the optical axis ("on-axis" laser beam), e.g. through the center of the injector's lens, the power is concentrated at the laser focal spot. When the laser beam does not exit through the center ("off axis" laser beam, with r the distance to the optical axis), the laser focal spot holds only a fraction of the total laser power. The ratio $R_P(r) = I(r) / I(0)$ between laser intensity at focal spot in on- and off-axis configurations was

measured on images of the laser spot exiting the injector (Supplementary. Fig. S11 A) using Image J by extracting the integral pixel value of the laser profile (cutoff at $1/e^2$ of maximum). The resulting energy per pulse off-axis can then be calculated: $E_p(r) = R_P(r) * P_0$.

For a given laser spot, beam radius at $1/e^2$ is calculated using a gaussian interpolation of the laser intensity profile (Supplementary. Fig. S11 B). In the on-axis configuration (r=0), laser radius is w_1 = 162 µm. Resulting power density is $P_1 = f_{rep} * E_{p1}/(\pi w_1^2)$, with E_{p1} = 15 µJ per pulse. P_1 = 1.11 W/mm². In the off-axis configuration (r = 300 µm), w_2 = 120 µm. The measured intensity ratio R_p (r) = 0.28 (Supplementary Fig. S11 C). As a result, for r = 300 µm, pulse energy at focal point is $E_{p2} = R_p(r) * E_{p1}$ = 4,2 µJ/pulse and power density $P_2 = E_{p2} / f_{rep}$ = 0.57 W/mm².

In this specific example, the power density is therefore approximately halved in the off-center position.

A

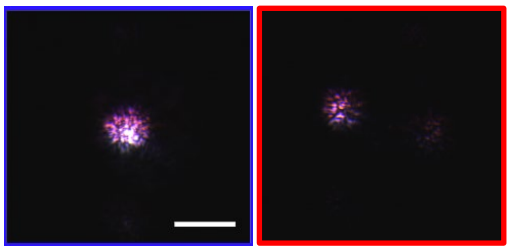

B

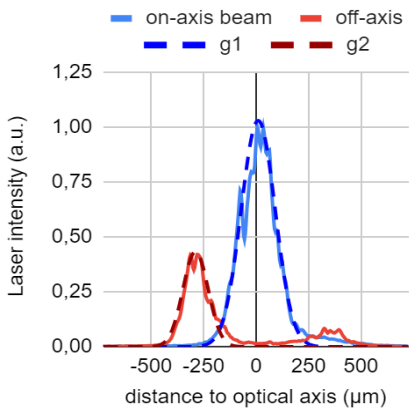

C

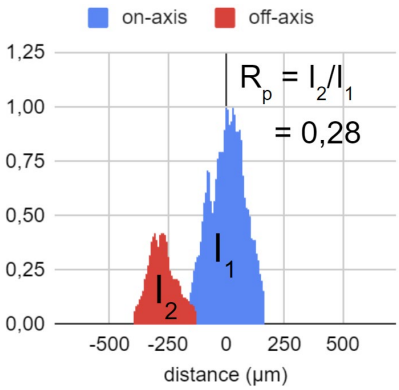

Supplementary Figure S11. **Estimation of laser power density exiting the laser injector** **(A)** Images of the 1030 nm laser beam exiting the injector. Left: on-axis beam, r=0. Right: off-axis beam, r = 300 µm. Scale bar: 500 µm. **(B)** Laser intensity profiles at focal spot of an on-axis and off-axis 1030 nm laser beam. Experimental profile (continuous line) and gaussian interpolations (dotted lines). **(C)** Integrals I_1 and I_2 (cutoff at $1/e^2$ of maximum) of the experimental laser profiles, respectively on-axis and off-axis.

Characterization of the laser beam on the retina / implant.

In the previous section, we estimated laser power density at focal point when the laser beam exits the laser injector off-axis. In practice, the rat retina is not in the focal plane of the injector lens during in vivo stimulations. When the PA implant or the rat retina is closer to the injector lens than the focal planes, the diameter D of the laser beam on the implant or retina will be larger than the laser spot diameter at the focal plane, whether the beam is off- or on-axis (Supplementary Fig. S12A). This will further reduce the laser power density.

When using a laser at repetition rate f_{rep} = 6.1 kHz and energy per pulse E_{p1} = 15 µJ/pulse, the resulting laser power density at focal plane (in an on-axis configuration) is $P_1 = f_{rep} * E_{p1}/(pi*w_1^2)$ = 1 W/mm², with w_1 = 162 µm as described in the previous section.

After placing the laser injector against the sedated rat's eye and taking a picture (eye fundus) of the laser beam, we experimentally measure a laser beam radius of w_2 = 195 µm (Supplementary Fig. S12B). This suggests that the retina is between the injector lens and its focal point. When using the same laser repetition rate (f_{rep} = 6.1 kHz) and energy per pulse (E_{p1} = 15 µJ/pulse), the resulting power density is P_{retina} = 0.69 W/mm².

Control experiments with a 595 nm and a 1030 nm laser used to directly stimulate the retina were all done in an on axis configuration. Experiments on implants had to be performed in off-axis configurations to perfectly align the laser on the 1 mm-diameter implant.

<u>Assumptions made to calculate laser power density (W/mm²) during stimulation on the retina or the implant.</u>

- for $E_P(r)$:
  - no light absorption in the eye (see justification below).
  - E_p = 15 µJ/pulse when the laser beam is on-axis.
  - no reflection of laser light on the implant. All the injected light is considered absorbed by the implant and converted into acoustic or thermal energy.
- The size of the imaged laser spot (on camera) is equal to the size of the spot on the PA implant.

In addition to optical aberrations due to the injector lens, we may also be witnessing spherical aberrations due to the biological lens[10].

A **B**

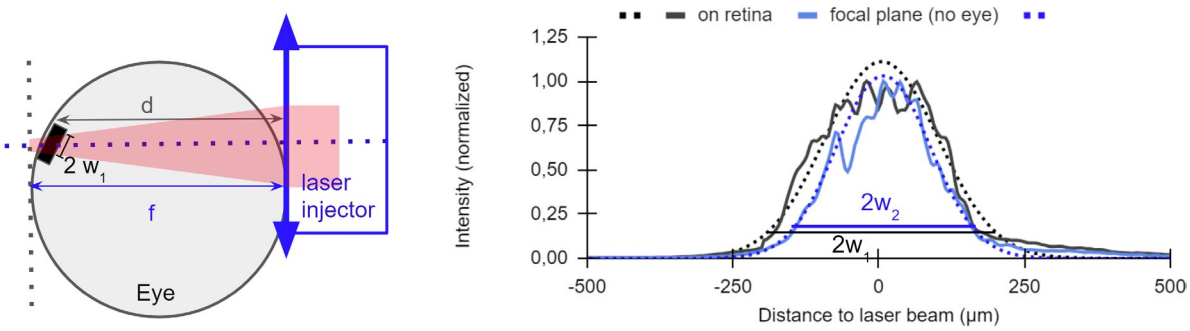

Supplementary Figure S12. **Estimation of the laser density on the retina or implant. (A)** Schematics of an injected laser beam in configuration where the injector lens' focal plane is behind the implant. f = 7 mm d < f. Laser spot diameter on implant D = $2w_1$. **(B)** Laser profiles (full line) obtained from eye fundus, and gaussian fits (dotted line) of on-axis laser beam at focal plane (blue trace) and on a rat retina (black). Laser diameter D = 2w, with laser beam radius a $1/e^2$.

The case for neglecting absorption in vivo

A rat's eye is 6.5 mm to 7 mm in diameter. Before reaching the implant, the 1030 nm laser light goes through the aqueous humor, the lens and the vitreous. At 1030 nm, the lens absorbs ~10% of laser energy[11]. Aqueous and the vitreous thickness in rats is much smaller than in humans (< 10 % for the vitreous). In humans, > 90% of 1030 nm light is transmitted through the aqueous and > 80 % through the vitreous[12]. Total light absorption by a rat's eye is therefore low enough (~ 20%) that we chose not to take it into account.

Bibliography

1. Chen, G. *et al.* High-precision neural stimulation by a highly efficient candle soot fiber optoacoustic emitter. *Front. Neurosci.* **16**, 1005810 (2022).
2. Wang, Q. *et al.* Thickness of individual layers at the macula and associated factors: the Beijing Eye Study 2011. *BMC Ophthalmol.* **20**, 49 (2020).
3. Menz, M. D. *et al.* Radiation Force as a Physical Mechanism for Ultrasonic Neurostimulation of the *Ex Vivo* Retina. *J. Neurosci.* **39**, 6251–6264 (2019).
4. Qu, Y. *et al.* Quantified elasticity mapping of retinal layers using synchronized acoustic radiation force optical coherence elastography. *Biomed. Opt. Express* **9**, 4054 (2018).
5. Menz, M. D., Oralkan, Ö., Khuri-Yakub, P. T. & Baccus, S. A. Precise Neural Stimulation in the Retina Using Focused Ultrasound. *J. Neurosci.* **33**, 4550–4560 (2013).
6. Zhuo, S.-Y. *et al.* Low-frequency, low-intensity ultrasound modulates light responsiveness of mouse retinal ganglion cells. *J. Neural Eng.* **19**, 046012 (2022).
7. Cherian, A. V. & Rau, K. R. Pulsed-laser-induced damage in rat corneas: time-resolved imaging of physical effects and acute biological response. *J. Biomed. Opt.* **13**, 024009 (2008).
8. Van Den Berg, T. J. T. P. & Spekreijse, H. Near infrared light absorption in the human eye media. *Vision Res.* **37**, 249–253 (1997).
9. Chen, P. *et al.* Acoustic characterization of tissue-mimicking materials for ultrasound perfusion imaging research. *Ultrasound Med. Biol.* **48**, 124–142 (2022).
10. Sivak, J. G. & Dovrat, A. Aging and the optical quality of the rat crystalline lens. *Invest. Ophthalmol. Vis. Sci.* **24**, 1162–1166 (1983).
11. Lei, B. & Yao, G. Spectral attenuation of the mouse, rat, pig and human lenses from wavelengths 360nm to 1020nm. *Exp. Eye Res.* **83**, 610–614 (2006).
12. Toadere, F. Comparative spectral analysis between the functionality of the human eye and of the optical part of a digital camera. in (eds. Cristea, I., Vladescu, M. & Tamas, R.) 92582T (Constanta, Romania, 2015). doi:10.1117/12.2071451.